

# OpenMIBOOD: Open Medical Imaging Benchmarks for Out-Of-Distribution Detection

Max Gutbrod<sup>1,2</sup>, David Rauber<sup>1</sup>, Danilo Weber Nunes<sup>1,2</sup>, Christoph Palm<sup>1,2</sup>

<sup>1</sup>Regensburg Medical Image Computing (ReMIC), OTH Regensburg, Regensburg, 93053, Germany

<sup>2</sup>Regensburg Center of Health Sciences and Technology (RCHST), OTH Regensburg, Regensburg, 93053, Germany

{max.gutbrod, christoph.palm}@oth-regensburg.de

## Abstract

*The growing reliance on Artificial Intelligence (AI) in critical domains such as healthcare demands robust mechanisms to ensure the trustworthiness of these systems, especially when faced with unexpected or anomalous inputs. This paper introduces the Open Medical Imaging Benchmarks for Out-Of-Distribution Detection (OpenMIBOOD), a comprehensive framework for evaluating out-of-distribution (OOD) detection methods specifically in medical imaging contexts. OpenMIBOOD includes three benchmarks from diverse medical domains, encompassing 14 datasets divided into covariate-shifted in-distribution, near-OOD, and far-OOD categories. We evaluate 24 post-hoc methods across these benchmarks, providing a standardized reference to advance the development and fair comparison of OOD detection methods. Results reveal that findings from broad-scale OOD benchmarks in natural image domains do not translate to medical applications, underscoring the critical need for such benchmarks in the medical field. By mitigating the risk of exposing AI models to inputs outside their training distribution, OpenMIBOOD aims to support the advancement of reliable and trustworthy AI systems in healthcare. The repository is available at <https://github.com/remic-othr/OpenMIBOOD>.*

## 1. Introduction

The rapid proliferation of AI systems in everyday life raises concerns about their trustworthiness. According to the technical specification ISO/IEC TS5723:2022 [30], an important aspect of trustworthiness concerns a system’s ability to handle unexpected inputs. Such inputs pose significant risks in safety-critical areas, including autonomous driving [11] and the healthcare sector [74]. Most AI systems are still trained and evaluated under the assumption that the training data distribution – referred to as in-distribution (ID) data – matches the distribution of data encountered post-

deployment. However, this assumption overlooks the possibility of encountering data from unknown and unseen distributions, known as out-of-distribution (OOD) data. When confronted with such data, AI models often exhibit high confidence in their predictions, even when these predictions are entirely incorrect [18]. Such behavior can result in silent and potentially catastrophic failures, particularly in high-stakes domains like healthcare, where erroneous predictions could directly impact patient safety. To address this, OOD detection methods help distinguish ID from OOD inputs, allowing models to flag or discard unreliable predictions or refer them for human review. Since 2016, numerous OOD detection methods have emerged [72], but a unified, comprehensive benchmark was lacking. Yang *et al.* addressed this by introducing OpenOOD [72], an open-source codebase that integrates related fields and provides a consistent evaluation framework.

In their framework, OOD is divided into two categories. The more challenging near-OOD, characterized by exhibiting similar semantics or styles compared to the ID datasets, making it particularly difficult to distinguish them. And the less challenging far-OOD, typically featuring different semantic labels and styles [16, 72].

In a follow-up version, OpenOOD v1.5 [77], Zhang *et al.* expanded their framework to encompass large-scale and full-spectrum OOD detection [73], covering over 50 methods. In this full-spectrum setting, the authors merged ID with covariate-shifted in-distribution (cs-ID) data – data, retaining the same labels and class relationships as the ID data while exhibiting variations in the distribution of input features. They argue that this approach evaluates not only OOD detection capabilities but also the generalization performance of an AI system. While this approach has undeniable value, we argue for analyzing OOD detection and model generalization independently to yield more precise insights. Furthermore, depending on the application, distinguishing between ID and cs-ID can be just as critical. For instance, in medical imaging, where training data is often limited or inaccessible due to privacy constraints, achieving

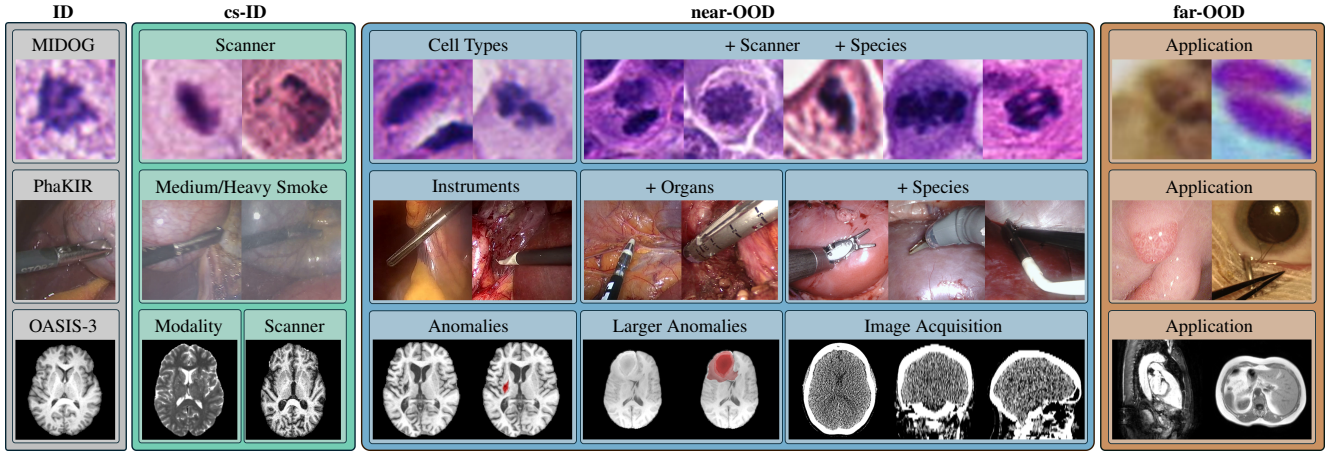


Figure 1. Illustration of all utilized datasets, categorized by varying degrees of domain shift, from cs-ID to near-OOD and far-OOD, presented from left to right: **MIDOG**: All distinct MIDOG domains [5], CCAgT [2, 4], FNAC 2019 [55]. **PhaKIR**: PhaKIR frames with smoke [53], Cholec80 [66], EndoSeg15 [10], EndoSeg18 [1], Kvasir-SEG [31, 50], CATARACTS [20]. **OASIS-3**: T2w modality and distinct scanner from OASIS-3 [38], ATLAS [43], Brats [47], CT from OASIS-3 [38], MSD-H [64], CHAOS [32]. On top of each group the primary domain shift is presented. A ‘+’ indicates that the previous domain shift is also included.

robust generalization may be challenging. In such cases, focusing on detecting cs-ID data can prove more impactful than solely aiming to enhance generalization performance.

We propose that, rather than combining ID and cs-ID data, OOD detection methods should be rigorously evaluated based on their capacity to differentiate between these two categories. This is particularly important in domains like healthcare, where the ability to identify subtle covariate shifts in data is essential to maintaining reliability.

To address the absence of medical images in the OpenOOD benchmark, we introduce three Medical Imaging Benchmarks (MIBs), which consist of 14 datasets organized into three distinct OOD evaluation settings named after their ID datasets: MIDOG [5], PhaKIR [53], and OASIS-3 [38]. An overview of these benchmarks and their involved domain shifts is provided in Fig. 1.

OOD detection methods are typically divided into two main types: post-hoc methods applied solely during inference, and methods requiring additional training steps. This work primarily focuses on post-hoc methods, valued for their ease of integration and model-agnostic nature. Besides these advantages, the analysis of Yang *et al.* showed that post-hoc methods are no worse than methods that require additional training steps [72].

Following an overview of the current benchmarks for OOD detection methods in the medical field (Sec. 2), we describe all evaluation settings, their underlying datasets, and the employed evaluation metrics (Sec. 3). Subsequently, we present the results of all evaluated methods, together with an in-depth discussion of these results (Sec. 4) and a summary of key findings and future research directions (Sec. 5).

Our main contributions are as follows:

- We introduce the most comprehensive OOD benchmarks for medical imaging across histopathology, endoscopy, and Magnetic Resonance Imaging (MRI) domains, evaluating 24 post-hoc methods and revealing gaps in current approaches for certain domain shifts in medical data.
- We show that selecting top-performing methods from benchmarks based on natural images likely leads to sub-optimal performance on medical imaging data.
- To reproduce our results, we provide a comprehensive codebase including all evaluated OOD detection methods, along with download links for the employed machine learning models and links to all utilized datasets.

## 2. Related Work

OOD detection is central to medical image processing, as it ensures that deep learning models can appropriately handle and respond to data that falls outside their training distribution. Despite its importance, only a limited number of publications have systematically evaluated OOD methods in this specific domain [12, 68, 79]. Instead, most studies have prioritized the development of new methods [27].

The Medical Out-of-Distribution Analysis Challenge [79] serves as a major benchmark for evaluating OOD and anomaly detection in medical images. Its ID datasets include MRI scans of healthy adults and Computed Tomography (CT) scans from patients over 50 years old referred for colonoscopy. The OOD test data feature synthetic image corruptions, alterations, and destructions, aligning with the cs-ID category of [77], as well as images of unseen medical conditions that correspond to near-OOD. The challenge results reveal a substantial variance in the

performance of OOD detection methods across different types of anomalies, indicating that none of the current approaches are sufficiently robust for immediate clinical deployment. However, this challenge has limitations: it does not comprehensively evaluate OOD detection methods across diverse medical imaging domains, nor does it offer a unified framework to guide and facilitate future research and development in the field.

Cao *et al.* [12] categorize OOD examples into three use cases: rejecting improperly preprocessed inputs (*i.e.* cs-ID), rejecting inputs that contain unseen conditions or artifacts (*i.e.* near-OOD), and rejecting unrelated inputs (*i.e.* far-OOD), such as cat pictures. Their evaluation spans eight post-hoc OOD detection methods and eight methods requiring additional training steps applied across three medical imaging contexts: chest X-ray, fundus imaging, and histology. However, the scope of their evaluation is notably limited, encompassing only basic post-hoc approaches. Additionally, the quality of the curated datasets presents challenges. For instance, evaluations involving natural images have limited relevance in a medical context. Furthermore, most evaluation settings rely on a single OOD dataset or even omit the essential context of near-OOD datasets.

In [68] the effectiveness of OOD detection methods is evaluated with a focus on medical 3D image segmentation. The ID datasets include CT images showing lung nodules and MRI images depicting benign brain tumors. Various OOD scenarios are evaluated, incorporating distribution shifts caused by different imaging devices and synthetic image corruptions (*i.e.* cs-ID), unseen diseases (*i.e.* near-OOD) and entirely different organs (*i.e.* far-OOD). The study evaluates three post-hoc methods and three methods that change the model architecture or training process. While the work contributes valuable insights into OOD detection within the context of 3D medical image segmentation, its scope remains limited. Notably, the study primarily emphasizes the evaluation of the author’s data-centric OOD detection method.

In addition to studies focusing on the evaluation of various OOD detection methods, Hong *et al.* [27] offer a comprehensive review of the OOD detection landscape within medical image analysis. They argue that the differentiation between cs-ID and near-OOD from OpenOOD is not entirely applicable for medical images. For example, while a classifier trained on X-ray images might still perform accurately on low-contrast X-rays, its performance is likely to degrade significantly when applied to entirely different modalities, such as CT scans [27]. Under the strict taxonomy outlined in [72, 77], both shifts would technically fall under the cs-ID category, as class labels remain unchanged, despite the significant differences in modality.

To address these limitations, Hong *et al.* propose an alternative taxonomy, categorizing domain shifts into covariate,

semantic, and contextual shifts. While this refinement offers greater precision, it does not account for certain semantic shifts, such as those observed across species in benchmarks like MIDOG and PhAKIR (Sec. 3). Consequently, this work adopts the established taxonomy of [72, 77] with a key modification: datasets with contextual differences from the ID data are classified as near-OOD if these differences are substantial enough to reasonably anticipate unreliable classification performance. This approach strikes the balance between the established taxonomy and the need for practical applicability in diverse medical imaging contexts.

### 3. OOD: Benchmarks and Metrics

To ensure reliable performance in machine learning models, robust control over their inputs is essential. OOD detection methods are designed to identify inputs that deviate significantly from a model’s training distribution, as such unfamiliar inputs can lead to unreliable predictions. The primary objective of OOD detection is to flag instances that fall outside the data distribution used during training. However, many existing OOD detection methods rely heavily on classification predictions, necessitating a highly effective underlying classification model for each ID dataset. The following subsection introduces the classification tasks and provides an overview of the datasets associated with them, highlighting their relevance to the evaluation of OOD detection approaches.

#### 3.1. Medical Imaging Benchmarks

This work builds upon the foundation of the existing OpenOOD benchmark [72–74, 77], which was originally developed for natural images. While following a similar structure and taxonomy, we extend this framework to the medical imaging domain by introducing OpenMIBOOD. To achieve this, we selected three datasets from diverse medical imaging fields as ID and curated corresponding cs-ID, near-OOD, and far-OOD datasets (Fig. 1). To ensure robust evaluation, all OOD datasets were further divided into validation and test sets. The validation sets are used for hyperparameter tuning, while the test sets were exclusively reserved for assessing OOD detection performance. Additional information on all datasets and their respective splits can be found in Appendix A.

**MIDOG** The MIDOG Challenge dataset [5] by Aubreville *et al.* comprises 503 images of Hematoxylin & Eosin stained histological whole slides. These images are organized into ten distinct domains, labeled as 1<sub>a-c</sub>, 2–5, 6<sub>a,b</sub>, and 7 (Appendix A.1), each exhibiting covariate shifts, semantic shifts, or both. These shifts arise from variations introduced by differing imaging hardware and staining protocols, as well as seven different cancer types from both human and canine species.

The dataset contains annotations for mitotic cells and mitotic cell lookalikes (imposters) in the form of  $50 \times 50$  px regions. To adapt the original object detection challenge into a three-class classification task, we utilized the provided annotations to create separate crops for mitotic cells and imposter cells. Moreover, we created additional crops by shifting each annotation window 100 px to the right, such that these crops do not belong to either of the original categories. These additional crops were subsequently used as training data for the third class. To ensure the quality and consistency of the dataset, crops smaller than  $50 \times 50$  px, typically occurring at the image borders, were excluded. Further, all additional crops overlapping with any annotation were also removed. The same procedure was applied to the remaining MIDOG dataset domains as well.

Since the primary distinction between the ID data and the data from domains  $1_b$  and  $1_c$  lies in the imaging devices used, we designated them as cs-ID.

The remaining domains of the MIDOG dataset were classified as near-OOD because they exhibit semantic shifts and, in most cases, additional covariate shifts.

For the far-OOD category, we incorporated two datasets associated with distinct medical applications. (1) **CCAgT dataset** [2, 4]: This dataset contains images of cervical cancer cells stained using the AgNOR technique, which specifically highlights regions within the cell nuclei. We utilized the available annotations of cell nuclei and extracted  $50 \times 50$  px crops centered on each nucleus. (2) **FNAC 2019 dataset** [55]: This dataset features Pap-stained images of breast FNAC samples. The crop extraction involved a binary threshold segmentation step, followed by a series of morphological operations to isolate cell clusters. From the processed images, the ten largest clusters were identified, and  $50 \times 50$  px crops were extracted at the centroids of these clusters.

**PhaKIR** The PhaKIR-Challenge dataset, introduced by Rueckert *et al.* [53], consists of eight publicly available real-world human cholecystectomy videos collected from three hospitals. It includes annotations for instance segmentation and keypoint detection of 19 distinct surgical instruments, as well as for intervention phases. To maintain consistency and to avoid introducing unintended covariate shifts, only the first six videos, containing a subset of ten surgical instruments and originating from a single hospital, are included in this study, while two videos from other hospitals are excluded. For this benchmark, we train a classification model to identify surgical instruments. Using the provided annotations, we selected 2769 frames containing only a single surgical instrument to simplify the classification task. Further, 1891 images that do not contain any instruments are also selected and classified under the category "No-Instrument".

To create separate ID and cs-ID datasets from the

PhaKIR-Challenge data, extracted frames were categorized into three smoke levels – none, medium, and heavy – based on the annotations from [54], reflecting the extent of smoke produced by tissue coagulation. Frames with no visible smoke were designated as the ID dataset, while frames with medium and heavy smoke were assigned to the cs-ID datasets. This separation ensures a clear distinction between the ID and the cs-ID datasets, enabling a robust evaluation of OOD detection performance with respect to covariate shifts caused by varying levels of smoke.

The following datasets were selected as near-OOD datasets, each introducing progressively greater semantic and covariate shifts. (1) **Cholec80 dataset** [66]: Although also featuring cholecystectomies, the instruments used differ from those in the ID dataset. Only those frames containing a single instrument were selected. Additionally, strong black vignettes present in almost all videos were removed by cropping a rectangular region within the vignette, preserving the original aspect ratio of the ID images. (2) **Instrument segmentation and tracking dataset (EndoSeg15)** [10]: From the Endoscopic Vision Challenge (EndoVis) 2015, this dataset includes frames from colorectal surgeries. We utilized images depicting rigid instruments that were distinct from those included in the ID dataset. (3) **Robotic scene segmentation dataset (EndoSeg18)** [1]: As part of the EndoVis Challenge 2018, this dataset features robotic instruments used in porcine nephrectomy procedures. To reduce the computational load, we utilized only the official test split from this dataset. Further, only the left frames from the stereo camera setup were used to maintain consistency with the other datasets. In contrast to the ID and Cholec80 datasets, we did not discard frames containing multiple instruments in EndoSeg15 and EndoSeg18.

For far-OOD evaluation, two datasets from entirely different medical fields were utilized: (1) **Kvasir-Seg dataset** [31]: This dataset consists of 1000 endoscopic images of polyps inside the bowel. (2) **CATARACTS dataset** [20]: Containing microscope videos of cataract surgeries, this dataset features a variety of ophthalmological instruments entirely different from those in the ID dataset.

**OASIS-3** The OASIS-3 [38] dataset comprises 2842 primarily high-resolution longitudinal MRI and low-dose CT scans from 1378 subjects, covering modalities such as T1-weighted (T1w), T2-weighted (T2w), and FLAIR. The dataset includes individuals ranging from cognitively normal (CN) to various stages of cognitive decline, up to Alzheimer's disease (AD). For this work, we specifically selected CN and AD subjects to facilitate a clearer distinction in brain tissue morphology. To ensure high-quality labels, we included only those MRI scans for which a clinical diagnosis is available within a 365-day window prior to the MRI acquisition date or a 182-day window after. If no diagnosis

was available within this constraints, the last one to three prior diagnoses were reviewed and accepted, provided they consistently indicated AD. All selected scans were preprocessed by resampling to an isotropic voxel spacing of  $1\text{ mm}^3$  and applying skull-stripping using HD-BET [29]. For the ID dataset, only T1w MRI scans were used to train a classification model to distinguish between CN and AD subjects. To evaluate the effects of covariate shifts, we created two cs-ID datasets: (1) **Modality-based covariate shift**: The first set comprises T2w MRI scans, introducing a covariate shift due to a change in imaging modality. (2): **Scanner-based covariate shift**: All T1w scans acquired using a Siemens Vision device were withheld to form the second cs-ID dataset, representing a shift in the MRI scanner.

The near-OOD category includes datasets that introduce varying degrees of domain shifts, ranging from subtle to more pronounced differences: (1) **ATLAS dataset** [43]: This dataset introduces a semantic shift as it contains images with stroke lesions, which differ from the CN and AD patterns in the ID dataset. Only T1w scans were selected, resampled, and skull-stripped to ensure consistency with the ID image properties. We excluded lower-quality scans to avoid introducing unintended covariate shifts (Appendix A.3). (2) **BraTS Challenge dataset** [6, 7, 47]: Featuring large gliomas that affect substantial regions of the brain, this dataset presents a more significant semantic shift compared to ATLAS. As with ATLAS, only T1w images were included, and no preprocessing was required. (3) **CT scans from OASIS-3**: These scans represent a unique near-OOD category. Although they depict the same subjects as the MRI scans, technically retaining the CN and AD labels, the acquisition method differs fundamentally. While CT scans are more sensitive to calcifications [78], atrophy is less visible [41], with both being relevant for the classification task. These differences can result in extracted features that may not align with those from MRI scans. To ensure only regions containing semantic shifts are evaluated, we discarded scans for both the ATLAS and the BraTS Challenge datasets where the pathological area lies outside the region of interest – a  $128\text{ mm}^3$  volume centered in the brain.

For the far-OOD setting, two datasets from entirely different anatomical regions were selected to introduce significant semantic and structural differences: (1) **Medical Segmentation Decathlon Heart (MSD-H) dataset** [3, 56, 64]: The MSD-H dataset includes high-resolution contrast-enhanced MRI scans of the heart captured during a single cardiac phase. (2) **CHAOS Challenge dataset** [32, 33]: We utilize the in-phase sequences from this dataset, which contains dual-echo MRI scans of the abdomen.

### 3.2. Metrics

We adopt the metrics established in the original OpenOOD framework [72, 77], treating OOD samples as the positive

class and use the area under the receiver operating characteristic curve (AUROC) as the primary metric to evaluate performance across all thresholds. It assesses the trade-off between the true positive rate (TPR) and false positive rate (FPR), measuring the model’s ability to separate ID from OOD. In addition, we employ the FPR@95 metric, measuring the FPR when 95 % of the ID data is correctly classified.

We also report the area under the Precision-Recall curve (AUPR) two variants: (1) with ID samples as the positive class ( $\text{AUPR}_{\text{IN}}$ ), to measure the model’s capacity to identify ID data; (2) with OOD samples as the positive class ( $\text{AUPR}_{\text{OUT}}$ ), to assess the model’s ability to detect unexpected inputs. Both AUPR metrics compute precision and recall across all classification thresholds, similar to AUROC. While we present all metric results in the supplementary (Appendix B.2), we report the harmonic mean of  $\text{AUPR}_{\text{IN}}$  and  $\text{AUPR}_{\text{OUT}}$  as a single, balanced metric for our main results. To better assess model performance in imbalanced settings, we replace OpenOOD’s [72, 77] accuracy metric with the F1-Score. Further details on the metric selection can be found in Appendix A.5.

## 4. Experiments and Results

This section begins by outlining the training pipeline for the classification models used with the three MIBs: MIDOG, PhaKIR, and OASIS-3. Subsequently, the conducted experiments are described and discussed in detail.

### 4.1. Classifier Training

All ID datasets are split into training, validation, and test subsets. To optimize the three MIB-specific classification models, we use the OneCycle learning rate scheduler [57] with either the SGD optimizer [63] for MIDOG and the Adam optimizer [36] for PhaKIR and OASIS-3. Final models, trained using cross-entropy loss, are selected based on the highest macro-averaged F1-score on the respective validation sets. To enhance performance and reduce training time, we initialize models with pre-trained weights without freezing any model parameters: ImageNet1k [14] for MIDOG and PhaKIR, and Kinetics400 [34] for OASIS-3. Appendix B.1 provides further details on each training setup.

### 4.2. Experimental Setup

We evaluate 24 post-hoc methods, initially evaluated on natural images, in the context of our MIBs, with results summarized in Tab. 1. The methods are ranked based on their average AUROC performance across all MIBs in the near-OOD setting, as this represents critical, high-risk scenarios where failure in OOD detection could lead to potential misdiagnoses or compromised patient safety.

We categorize the evaluated methods into three groups:

(1) **Classification-Based Methods (blue)**: These methods primarily use information derived from the model output

Table 1. Results of all evaluated OOD detection methods, ranked by their average performance (AUROC) across all MIB groups for the **near-OOD** category. Additionally, the table includes the averaged near-OOD performance based on the harmonic mean of AUPR<sub>IN</sub> and AUPR<sub>OUT</sub>, as well as the averaged FPR@95 metrics. The F1-Score indicates the performance on the ID test set. Rows are color-coded to indicate the source of information used for OOD detection: blue for probabilities or logits, orange for feature space, and green for a combination of both. \*: The results of the MDSEns method are potentially misleading, as discussed in the main text (Sec. 4.3).

	MIDOG @ F1-Score: 81.88			PhaKIR @ F1-Score: 80.08			OASIS-3 @ F1-Score: 73.65			Averages for near-OOD		
	cs-ID	near-OOD	far-OOD	cs-ID	near-OOD	far-OOD	cs-ID	near-OOD	far-OOD	AUROC↑	AUPR↑	FPR@95↓
MDSEns* [40]	99.19	91.84	100.00	65.05	97.11	98.50	100.00	99.46	100.00	96.14	91.86	11.97
ViM [70]	59.73	62.67	84.78	72.39	81.14	55.34	98.82	98.40	100.00	80.74	70.21	48.79
Residual [70]	60.26	65.78	92.35	57.12	76.99	57.31	96.97	96.70	100.00	79.82	70.18	49.94
MDS [40]	58.60	63.21	90.91	56.04	76.48	51.47	96.31	96.15	100.00	78.61	69.72	51.29
KNN [61]	57.97	61.63	90.18	34.05	55.44	37.75	98.78	97.66	100.00	71.58	61.94	62.62
SHE [76]	57.89	61.80	91.09	36.18	50.34	47.40	91.85	90.80	99.64	67.65	58.40	67.29
RMDS [52]	49.46	52.23	60.68	38.22	67.73	35.49	58.00	71.69	99.89	63.88	48.58	79.88
Relation [35]	55.68	58.71	86.17	31.06	61.02	30.72	45.48	66.20	92.91	61.98	47.95	78.62
fDBD [44]	52.54	58.33	83.03	30.08	50.13	27.54	58.62	75.31	92.93	61.26	50.33	76.55
SCALE [71]	53.44	55.71	82.03	35.91	38.97	46.83	84.53	84.32	98.23	59.67	48.91	78.67
ReAct [60]	53.79	57.40	84.86	30.34	48.38	25.89	44.74	70.23	77.53	58.67	46.49	81.79
ASH [15]	53.93	56.02	82.70	45.99	40.17	65.08	70.71	76.52	91.48	57.57	46.13	80.71
RankFeat [58]	48.17	51.83	56.44	52.01	45.26	27.35	71.29	74.65	96.99	57.25	48.14	80.36
OpenMax [8]	49.88	52.75	65.87	31.90	66.03	33.56	43.69	52.60	70.47	57.13	40.39	90.03
ODIN [42]	56.38	61.37	85.08	34.28	41.78	71.82	53.51	59.53	58.63	54.23	44.15	86.91
GEN [46]	52.54	55.46	79.78	32.65	51.55	32.68	36.95	53.50	78.45	53.50	37.50	91.64
MSP [23]	53.37	55.90	80.91	32.04	50.16	32.51	36.95	53.50	78.45	53.19	37.29	91.71
Dropout [17]	53.25	55.76	80.87	31.96	50.10	32.56	37.10	53.22	77.13	53.03	37.17	91.88
TempScale [19]	53.57	56.05	81.38	31.73	48.73	32.50	36.95	53.50	78.45	52.76	37.05	91.65
NNGuide [49]	58.08	59.84	89.58	29.15	37.98	40.94	34.76	56.95	76.37	51.59	37.08	90.55
KLM [24]	48.34	51.54	73.53	55.15	56.34	35.87	54.51	44.49	63.98	50.79	36.57	89.40
EBO [45]	54.46	56.85	84.45	31.99	40.18	34.34	33.86	49.39	69.65	48.81	35.23	92.33
MLS [26]	54.22	56.58	82.98	32.00	40.17	34.33	33.94	49.47	69.73	48.74	35.22	92.37
DICE [59]	51.56	54.15	79.08	35.96	53.33	22.65	34.66	26.14	23.70	44.54	34.22	92.83

probabilities or logits. (2) **Feature-Based Methods (orange)**: These methods rely exclusively on information from the feature space. (3) **Hybrid Methods (green)**: These methods combine both sources of information.

For this evaluation, we extend the codebase provided by the OpenOOD benchmark [77]. To enable hyperparameter tuning, we aggregate validation splits from all near-OOD datasets within each benchmark. Fine-tuning is conducted on this combined validation set, focusing on optimizing performance in the challenging near-OOD context.

### 4.3. Results on all Medical Imaging Benchmarks

In this subsection we start with a description of the four top-performing methods, followed by a detailed analysis of the challenges posed by specific datasets to those methods. It also addresses the suboptimal performance of classification-based methods and compares the results with those obtained on the ImageNet1k benchmark from OpenOOD [72]. Additionally, Table 8 – Tab. 10 in the appendix provide concise summaries of all the approaches.

**MDSEns and MDS** The MDSEns method [40] from Lee *et al.* achieved the best overall performance across all MIBs. This method calculates the Mahalanobis distance between feature embeddings of test samples and precomputed class-conditional Gaussian distributions derived from ID training data across multiple model layers. MDSEns aggregates

these distance calculations from all intermediate layers through weighted averaging, with weights optimized during an initial setup phase using logistic regression on validation data containing both ID and OOD examples.

In contrast to MDSEns, the fourth-ranked method MDS [40] computes the Mahalanobis distance using feature embeddings derived solely from the penultimate layer.

**Residual and ViM** Similar to MDS, the third-ranked method Residual from Wang *et al.* [70] relies entirely on features extracted from the penultimate layer. The method projects features onto a low-variance subspace defined by the  $N$  smallest eigenvalues of the empirical covariance matrix calculated from all ID training data, and uses the norm of those features as the OOD score.

ViM, an extension of the Residual method, integrates class-specific logit information to enhance OOD detection [70]. It achieves this by transforming the Residual output into a virtual logit, which is then combined with Energy-Based OOD Detection (EBO) [45]. This approach recovers information lost in the feature-to-logit mapping, consistently improving detection performance across diverse OOD scenarios with natural images.

**Results on challenging datasets** Figure 2 illustrates the distribution of OOD scores and corresponding AUROC values for the four top-performing methods on particularly

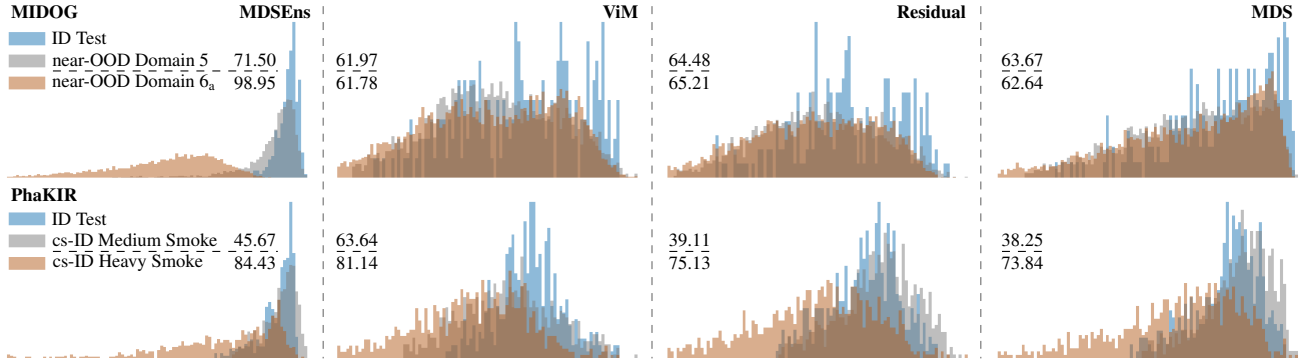


Figure 2. Distribution of OOD scores for the top four methods on challenging datasets from the MIDOG and PhaKIR benchmarks, including AUROC values for each dataset and method.

challenging datasets from MIDOG and PhaKIR. A corresponding visualization for OASIS-3 is presented in Fig. 4 in the appendix. From Tab. 1 it is evident that MDSEns delivers strong overall performance across the evaluated MIBs. However, even this top-performing method faces difficulties in reliably distinguishing between ID and OOD data under certain challenging conditions, such as given by MIDOG’s domain 5 dataset and PhaKIR’s Medium Smoke dataset.

This outcome aligns with the characteristics of domain 5 from MIDOG, which originates from the same scanner and institution as the ID data. Here, the primary shift is semantic, involving a different cell type from the same species. In contrast, domain 6<sub>a</sub> exhibits both a more pronounced semantic shift – a different cell type from another species – and additional covariate shifts introduced by variations in scanner type and institution. While MDSEns achieves near-perfect separation in domain 6<sub>a</sub>, where both semantic and covariate shifts are present, it degrades significantly in domain 5, where only a semantic shift is involved.

This finding indicates that MDSEns’ strong performance is heavily influenced by its ability to detect covariate shifts, which are often more prominent in the datasets used. MDSEns uniquely uses information from early intermediate layers of the network, where covariate shifts are more likely to manifest as changes in basic features like edges, shapes, and colors [37, 75]. This observation aligns with prior findings [68], demonstrating that simple approaches based on input intensity distributions can yield results comparable to methods that rely on deeper network layers or final outputs.

For the PhaKIR Medium Smoke dataset, the overlap between OOD and ID scores can be attributed to the subtle appearance of smoke in the images. Often, the smoke is limited to regions that do not contain instruments. Given that the model’s primary task is instrument classification, it likely prioritizes regions containing instruments over background areas. As a result, features associated with smoke, particularly in non-instrument regions, are minimally en-

coded. A representative example of this behavior is shown in Fig. 5 in the appendix. If the downstream task were instead organ classification, it is likely that smoke would have a stronger impact on the encoded features, as it could obscure or alter key characteristics of the organs themselves.

Comparing the performance of Residual and ViM [70] on PhaKIR’s cs-ID Medium Smoke dataset reveals significant performance degradation (Fig. 2) for ViM. While Residual performs robustly in this scenario, ViM, which combines Residual with the EBO method [45], exhibits a noticeable drop in performance. This degradation is explained by EBO’s poor performance on this dataset, with an AUROC of 23.74.

**Poor performance of classification-based methods** An evaluation of the average AUROC for classification-based approaches across the three MIBs reveals a significant lack of discriminative power compared to feature-based methods (Tab. 7 in the appendix). These approaches inherently rely on the assumption that ID data should yield higher confidence scores than OOD data. However, this assumption is often violated in practice, as demonstrated by our analysis.

For example, in the PhaKIR benchmark, the mean softmax probability for ID predictions of the “Grasper” class is 79.07 %, whereas for OOD predictions from the EndoSeg18 dataset, the mean probability on all Grasper predictions increases to 94.04 %. This paradoxical result indicates a critical flaw: the classifier overconfidently assigns the Grasper label to OOD data. Analyzing the feature space reveals that OOD data from EndoSeg18 clusters predominantly near the Grasper class (Fig. 6 in the appendix), suggesting a bias in the classifier toward assigning this label to instruments that do not clearly belong to any other class. Together, these factors explain the low average AUROC of 33.71 for classification-based methods on the EndoSeg18 dataset.

Similar patterns of poor discrimination are observed across other datasets. In the Kvasir-SEG dataset, for ex-

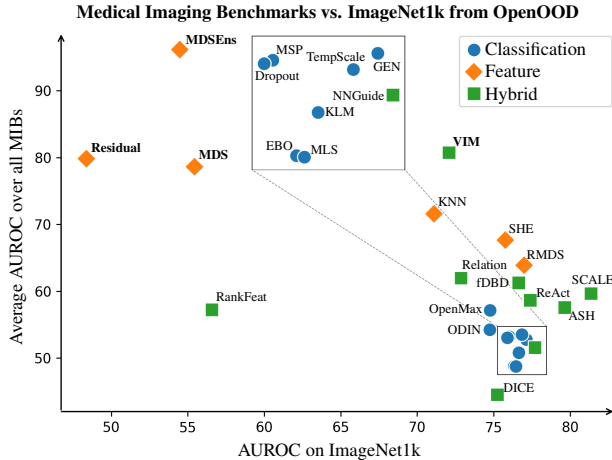


Figure 3. Average ranking of each method based on AUROC across the MIBs (y-axis) and on the ImageNet1k benchmark (x-axis).

ample, the classifier assigned higher scores to predictions for the "No-Instrument" class than it did for ID data. Similarly, in the OASIS-3 benchmark, outputs for the CN class are nearly identical between the ID and the ATLAS dataset, compromising the ability of classification-based methods to distinguish between ID and OOD samples in each case.

#### Comparison with OpenOOD’s ImageNet1k benchmark

Figure 3 compares the average AUROC across the MIBs for all evaluated methods with their performance on the ImageNet1k benchmark from OpenOOD [72]. The results highlight that no single method fully addresses the challenge of OOD detection across both natural and medical imaging scenarios. The closest contender of a comprehensive approach is ViM, which combines information from both feature space and the classification layers. ViM achieves an average AUROC of 80.74 on the MIBs and 72.08 on the ImageNet1k benchmark, demonstrating its adaptability to different domains. However, the performance gap between these benchmarks underscores the complexity and specificity of OOD detection in medical imaging, where domain characteristics significantly differ from those of natural images. Notably, methods that rely primarily on feature space information tend to perform better on medical images, while methods leveraging probabilities or logits show superior results on natural images. This discrepancy may stem from the lower variance typically observed in medical images compared to natural images. For instance, the average standard deviation in pixel intensity is 0.148/0.149 for the MIDOG/PhaKIR ID datasets, respectively, compared to 0.226 for the ImageNet1k dataset. The lower variance in medical images, along with the typically small number of target classes in medical datasets, may re-

sult in more cohesive and less fragmented feature spaces, thereby enhancing the effectiveness of feature-based methods for detecting OOD samples, presenting a starting point for future research. On the other hand, natural images, with their higher variability and richer textures, likely benefit from methods that exploit class probabilities and logits. Detailed results on ImageNet1k can be found in Appendix B.2.

## 5. Conclusion

In this work, we introduced the Open Medical Imaging Benchmarks for Out-Of-Distribution Detection (OpenMIBOOD), representing a significant step forward in the evaluation and development of OOD detection methods for medical imaging. OpenMIBOOD comprises a comprehensive set of three benchmarks consisting of 14 datasets, categorized into in-distribution, covariate-shifted in-distribution, near-OOD, and far-OOD. Across these benchmarks, we evaluated 24 post-hoc OOD detection methods and analyzed their performance and limitations in the medical field.

Our results reveal that state-of-the-art OOD detection methods that rely on feature space information consistently outperform methods that depend solely on probabilities and logits when applied to medical datasets. However, our findings also highlight a critical challenge: methods originally designed and optimized for natural images often fail to generalize to medical data. This underscores the need for tailored solutions that address the unique characteristics of medical imaging, such as lower variance, domain-specific semantic shifts, and imbalanced datasets. The precise reasons behind these discrepancies remain an area for further research. One notable limitation of our benchmark is its focus on classification tasks, which limits the applicability of our findings to such problems. Future work could extend the evaluation framework to seamlessly include segmentation tasks, a critical component of medical imaging, by adapting the included OOD detection methods to operate in segmentation settings. While we focus on evaluating OOD detection methods using deep Neural Networks, we recognize the potential of other approaches. For example, analyzing and evaluating input data distributions and directly comparing them to training set distributions could complement Neural Network-based OOD detection.

As Artificial Intelligence continues to advance in the medical field, the insights and benchmarks provided by OpenMIBOOD will play a vital role in driving innovation. By exposing the strength and weaknesses of existing methods and setting a high standard for future development, OpenMIBOOD contributes to the creation of trustworthy AI systems. These systems will be essential for safely and effectively addressing the challenges of clinical application, ensuring that AI technologies enhance patient care while maintaining high standards of reliability and safety.

## References

[1] Max Allan, Satoshi Kondo, Sebastian Bodenstedt, Stefan Leger, Rahim Kadkhodamohammadi, Imanol Luengo, Felix Fuentes, Evangello Flouty, Ahmed Mohammed, Marius Pedersen, et al. 2018 Robotic Scene Segmentation Challenge. *ArXiv preprint*, abs/2001.11190, 2020. [2](#), [4](#)

[2] João Gustavo Atkinson Amorim, Luiz Antonio Buschetto Macarini, André Victória Matias, Allan Cerentini, Fabiana Botelho De Miranda Onofre, Alexandre Sherley Casimiro Onofre, and Aldo Von Wangenheim. A novel approach on segmentation of agnor-stained cytology images using deep learning. In *Proceedings of the 2020 IEEE 33rd International Symposium on Computer-Based Medical Systems (CBMS)*, pages 552–557. IEEE, 2020. [2](#), [4](#), [1](#)

[3] Michela Antonelli, Annika Reinke, Spyridon Bakas, Keyvan Farahani, Annette Kopp-Schneider, Bennett A Landman, Geert Litjens, Bjoern Menze, Olaf Ronneberger, Ronald M Summers, et al. The medical segmentation decathlon. *Nature communications*, 13(1):4128, 2022. [5](#), [3](#)

[4] João Gustavo Atkinson Amorim, André Matias, Tainee Bottamedi, Vinícius Sanches, Ane Francyne Costa, Fabiana Onofre, Alexandre Onofre, and Aldo Wangenheim. CCAgT: Images of Cervical Cells with AgNOR Stain Technique, 2022. Accessed: 2024-10-13, Publisher: Mendeley Data. [2](#), [4](#), [1](#)

[5] Marc Aubreville, Frauke Wilm, Nikolas Stathonikos, Katharina Breininger, Taryn A Donovan, Samir Jabari, Mitko Veta, Jonathan Ganz, Jonas Ammeling, Paul J van Diest, et al. A comprehensive multi-domain dataset for mitotic figure detection. *Scientific data*, 10(1):484, 2023. [2](#), [3](#), [1](#)

[6] Ujjwal Baid, Satyam Ghodasara, Suyash Mohan, Michel Bilello, Evan Calabrese, Errol Colak, Keyvan Farahani, Jayashree Kalpathy-Cramer, Felipe C Kitamura, Sarthak Pati, et al. The RSNA-ASNR-MICCAI BraTS 2021 Benchmark on Brain Tumor Segmentation and Radiogenomic Classification. *ArXiv preprint*, abs/2107.02314, 2021. [5](#), [3](#)

[7] Spyridon Bakas, Hamed Akbari, Aristeidis Sotiras, Michel Bilello, Martin Rozycki, Justin S Kirby, John B Freymann, Keyvan Farahani, and Christos Davatzikos. Advancing the Cancer Genome Atlas Glioma MRI Collections with Expert Segmentation Labels and Radiomic Features. *Scientific data*, 4(1):1–13, 2017. [5](#), [3](#)

[8] Abhijit Bendale and Terrance E. Boult. Towards Open Set Deep Networks. In *2016 IEEE Conference on Computer Vision and Pattern Recognition, CVPR 2016, Las Vegas, NV, USA, June 27-30, 2016*, pages 1563–1572. IEEE Computer Society, 2016. [6](#), [8](#), [10](#), [11](#), [12](#), [13](#), [14](#), [15](#), [16](#), [17](#)

[9] Julian Bitterwolf, Maximilian Müller, and Matthias Hein. In or Out? Fixing ImageNet Out-of-Distribution Detection Evaluation. In *International Conference on Machine Learning, ICML 2023, 23-29 July 2023, Honolulu, Hawaii, USA*, pages 2471–2506. PMLR, 2023. [16](#), [17](#)

[10] Sebastian Bodenstedt, Max Allan, Anthony Agustinos, Xiaofei Du, Luis Garcia-Peraza-Herrera, Hannes Kenngott, Thomas Kurmann, Beat Müller-Stich, Sébastien Ourselin, Daniil Pakhomov, et al. Comparative Evaluation of Instrument Segmentation and Tracking Methods in Minimally Invasive Surgery. *ArXiv preprint*, abs/1805.02475, 2018. [2](#), [4](#)

[11] Daniel Bogdol, Maximilian Nitsche, and J. Marius Zöllner. Anomaly Detection in Autonomous Driving: A Survey. In *IEEE/CVF Conference on Computer Vision and Pattern Recognition Workshops, CVPR Workshops 2022, New Orleans, LA, USA, June 19-20, 2022*, pages 4487–4498. IEEE, 2022. [1](#)

[12] Tianshi Cao, Chin-Wei Huang, David Yu-Tung Hui, and Joseph Paul Cohen. A benchmark of medical out of distribution detection. *ArXiv preprint*, abs/2007.04250, 2020. [2](#), [3](#)

[13] Mircea Cimpoi, Subhransu Maji, Iasonas Kokkinos, Sammy Mohamed, and Andrea Vedaldi. Describing Textures in the Wild. In *2014 IEEE Conference on Computer Vision and Pattern Recognition, CVPR 2014, Columbus, OH, USA, June 23-28, 2014*, pages 3606–3613. IEEE Computer Society, 2014. [16](#), [17](#)

[14] Jia Deng, Wei Dong, Richard Socher, Li-Jia Li, Kai Li, and Fei-Fei Li. Imagenet: A large-scale hierarchical image database. In *2009 IEEE Computer Society Conference on Computer Vision and Pattern Recognition (CVPR 2009), 20-25 June 2009, Miami, Florida, USA*, pages 248–255. IEEE Computer Society, 2009. [5](#)

[15] Andrija Djurisic, Nebojsa Bozanic, Arjun Ashok, and Rosanne Liu. Extremely Simple Activation Shaping for Out-of-Distribution Detection. In *The Eleventh International Conference on Learning Representations, ICLR 2023, Kigali, Rwanda, May 1-5, 2023*. OpenReview.net, 2023. [6](#), [9](#), [10](#), [11](#), [12](#), [13](#), [14](#), [15](#), [16](#), [17](#)

[16] Zhen Fang, Yixuan Li, Jie Lu, Jiahua Dong, Bo Han, and Feng Liu. Is Out-of-Distribution Detection Learnable? In *Advances in Neural Information Processing Systems 35: Annual Conference on Neural Information Processing Systems 2022, NeurIPS 2022, New Orleans, LA, USA, November 28 - December 9, 2022*, 2022. [1](#)

[17] Yarin Gal and Zoubin Ghahramani. Dropout as a Bayesian Approximation: Representing Model Uncertainty in Deep Learning. In *Proceedings of the 33rd International Conference on Machine Learning, ICML 2016, New York City, NY, USA, June 19-24, 2016*, pages 1050–1059. JMLR.org, 2016. [6](#), [8](#), [10](#), [11](#), [12](#), [13](#), [14](#), [15](#), [16](#), [17](#)

[18] Ian J. Goodfellow, Jonathon Shlens, and Christian Szegedy. Explaining and Harnessing Adversarial Examples. In *3rd International Conference on Learning Representations, ICLR 2015, San Diego, CA, USA, May 7-9, 2015, Conference Track Proceedings*, 2015. [1](#)

[19] Chuan Guo, Geoff Pleiss, Yu Sun, and Kilian Q. Weinberger. On Calibration of Modern Neural Networks. In *Proceedings of the 34th International Conference on Machine Learning, ICML 2017, Sydney, NSW, Australia, 6-11 August 2017*, pages 1321–1330. PMLR, 2017. [6](#), [8](#), [10](#), [11](#), [12](#), [13](#), [14](#), [15](#), [16](#), [17](#)

[20] Hassan Al Hajj, Mathieu Lamard, Pierre-Henri Conze, Soumali Roychowdhury, Xiaowei Hu, Gabija Marsalkaitė, Odysseas Zisiopoulos, Muneer Ahmad Dedmari, Fenqiang Zhao, Jonas Prellberg, Manish Sahu, Adrian Galdran, Teresa

Araújo, Duc My Vo, Chandan Panda, Navdeep Dahiya, Satoshi Kondo, Zhengbing Bian, and Gwenolé Quellec. CATARACTS: challenge on automatic tool annotation for cataract surgery. *Medical Image Anal.*, 52:24–41, 2019. [2](#), [4](#)

[21] Kaiming He, Xiangyu Zhang, Shaoqing Ren, and Jian Sun. Deep Residual Learning for Image Recognition. In *2016 IEEE Conference on Computer Vision and Pattern Recognition, CVPR 2016, Las Vegas, NV, USA, June 27-30, 2016*, pages 770–778. IEEE Computer Society, 2016. [5](#)

[22] Dan Hendrycks and Thomas G. Dietterich. Benchmarking Neural Network Robustness to Common Corruptions and Perturbations. In *7th International Conference on Learning Representations, ICLR 2019, New Orleans, LA, USA, May 6-9, 2019*. OpenReview.net, 2019. [16](#), [17](#)

[23] Dan Hendrycks and Kevin Gimpel. A Baseline for Detecting Misclassified and Out-of-Distribution Examples in Neural Networks. In *5th International Conference on Learning Representations, ICLR 2017, Toulon, France, April 24-26, 2017, Conference Track Proceedings*. OpenReview.net, 2017. [6](#), [8](#), [10](#), [11](#), [12](#), [13](#), [14](#), [15](#), [16](#), [17](#)

[24] Dan Hendrycks, Steven Basart, Mantas Mazeika, Mohammadreza Mostajabi, Jacob Steinhardt, and Dawn Song. A Benchmark for Anomaly Segmentation. *ArXiv preprint*, abs/1911.11132, 2019. [6](#), [8](#), [10](#), [11](#), [12](#), [13](#), [14](#), [15](#), [16](#), [17](#)

[25] Dan Hendrycks, Steven Basart, Norman Mu, Saurav Kadavath, Frank Wang, Evan Dorundo, Rahul Desai, Tyler Zhu, Samyak Parajuli, Mike Guo, Dawn Song, Jacob Steinhardt, and Justin Gilmer. The Many Faces of Robustness: A Critical Analysis of Out-of-Distribution Generalization. In *2021 IEEE/CVF International Conference on Computer Vision, ICCV 2021, Montreal, QC, Canada, October 10-17, 2021*, pages 8320–8329. IEEE, 2021. [16](#), [17](#)

[26] Dan Hendrycks, Steven Basart, Mantas Mazeika, Andy Zou, Joseph Kwon, Mohammadreza Mostajabi, Jacob Steinhardt, and Dawn Song. Scaling Out-of-Distribution Detection for Real-World Settings. In *International Conference on Machine Learning, ICML 2022, 17-23 July 2022, Baltimore, Maryland, USA*, pages 8759–8773. PMLR, 2022. [6](#), [8](#), [10](#), [11](#), [12](#), [13](#), [14](#), [15](#), [16](#), [17](#)

[27] Zesheng Hong, Yubiao Yue, Yubin Chen, Huanjie Lin, Yuanmei Luo, Mini Han Wang, Weidong Wang, Jialong Xu, Xiaoli Yang, Zhenzhang Li, et al. Out-of-distribution Detection in Medical Image Analysis: A survey. *ArXiv preprint*, abs/2404.18279, 2024. [2](#), [3](#)

[28] Grant Van Horn, Oisin Mac Aodha, Yang Song, Yin Cui, Chen Sun, Alexander Shepard, Hartwig Adam, Pietro Perona, and Serge J. Belongie. The INaturalist Species Classification and Detection Dataset. In *2018 IEEE Conference on Computer Vision and Pattern Recognition, CVPR 2018, Salt Lake City, UT, USA, June 18-22, 2018*, pages 8769–8778. IEEE Computer Society, 2018. [16](#), [17](#)

[29] Fabian Isensee, Marianne Schell, Irada Pflueger, Gianluca Brugnara, David Bonekamp, Ulf Neuberger, Antje Wick, Heinz-Peter Schlemmer, Sabine Heiland, Wolfgang Wick, et al. Automated brain extraction of multisequence MRI using artificial neural networks. *Human brain mapping*, 40(17):4952–4964, 2019. [5](#), [3](#)

[30] ISO. *ISO/IEC TS5723:2022: Trustworthiness — Vocabulary*. International Organization for Standardization, Geneva, Switzerland, 2022. [1](#)

[31] Debesh Jha, Pia H Smedsrød, Michael A Riegler, Pål Halvorsen, Thomas De Lange, Dag Johansen, and Håvard D Johansen. Kvasir-seg: A segmented polyp dataset. In *MultiMedia modeling: 26th international conference, MMM 2020, Daejeon, South Korea, January 5–8, 2020, proceedings, part II* 26, pages 451–462. Springer, 2020. [2](#), [4](#)

[32] Ali Emre Kavur, M. Alper Selver, Oğuz Dicle, Mustafa Barış, and N. Sinem Gezer. CHAOS - Combined (CT-MR) Healthy Abdominal Organ Segmentation Challenge Data, 2019. [2](#), [5](#), [3](#)

[33] A. Emre Kavur, Naciye Sinem Gezer, Mustafa Baris, Sinem Aslan, Pierre-Henri Conze, Vladimir Groza, Duc Duy Pham, Soumick Chatterjee, Philipp Ernst, Savas Özkan, Bora Baydar, Dmitry A. Lachinov, Shuo Han, Josef Pauli, Fabian Isensee, Matthias Perkonigg, Rachana Sathish, Ronnie Rajan, Debdoot Sheet, Gurbandurdy Dovletov, Oliver Speck, Andreas Nürnberger, Klaus H. Maier-Hein, Gözde B. Akar, Gözde B. Ünal, Oğuz Dicle, and M. Alper Selver. CHAOS Challenge - combined (CT-MR) healthy abdominal organ segmentation. *Medical Image Anal.*, 69:101950, 2021. [5](#), [3](#)

[34] Will Kay, Joao Carreira, Karen Simonyan, Brian Zhang, Chloe Hillier, Sudheendra Vijayanarasimhan, Fabio Viola, Tim Green, Trevor Back, Paul Natsev, et al. The kinetics human action video dataset. *ArXiv preprint*, abs/1705.06950, 2017. [5](#)

[35] Jang-Hyun Kim, Sangdoo Yun, and Hyun Oh Song. Neural Relation Graph: A Unified Framework for Identifying Label Noise and Outlier Data. In *Advances in Neural Information Processing Systems 36: Annual Conference on Neural Information Processing Systems 2023, NeurIPS 2023, New Orleans, LA, USA, December 10 - 16, 2023*, 2023. [6](#), [9](#), [10](#), [11](#), [12](#), [13](#), [14](#), [15](#), [16](#), [17](#)

[36] Diederik P. Kingma and Jimmy Ba. Adam: A Method for Stochastic Optimization. In *3rd International Conference on Learning Representations, ICLR 2015, San Diego, CA, USA, May 7-9, 2015, Conference Track Proceedings*, 2015. [5](#)

[37] Alex Krizhevsky, Ilya Sutskever, and Geoffrey E. Hinton. Imagenet Classification with Deep Convolutional Neural Networks. In *Advances in Neural Information Processing Systems 25: 26th Annual Conference on Neural Information Processing Systems 2012. Proceedings of a meeting held December 3-6, 2012, Lake Tahoe, Nevada, United States*, pages 1106–1114, 2012. [7](#)

[38] Pamela J LaMontagne, Tammie LS Benzinger, John C Morris, Sarah Keefe, Russ Hornbeck, Chengjie Xiong, Elizabeth Grant, Jason Hassenstab, Krista Moulder, Andrei G Vlassenko, et al. Oasis-3: longitudinal neuroimaging, clinical, and cognitive dataset for normal aging and Alzheimer disease. *medrxiv*, pages 2019–12, 2019. [2](#), [4](#), [3](#)

[39] Yann LeCun, Sumit Chopra, Raia Hadsell, M Ranzato, Fujie Huang, et al. A Tutorial on Energy-Based Learning. *Predicting structured data*, 1(0), 2006. [8](#)

[40] Kimin Lee, Kibok Lee, Honglak Lee, and Jinwoo Shin. A Simple Unified Framework for Detecting Out-of-

Distribution Samples and Adversarial Attacks. In *Advances in Neural Information Processing Systems 31: Annual Conference on Neural Information Processing Systems 2018, NeurIPS 2018, December 3-8, 2018, Montréal, Canada*, pages 7167–7177, 2018. 6, 8, 10, 11, 12, 13, 14, 15, 16, 17

[41] Robert M Levy, Catherine M Mills, Jonathan P Posin, Sheila G Moore, Mark L Rosenblum, and Dale E Bredesen. The efficacy and clinical impact of brain imaging in neurologically symptomatic AIDS patients: a prospective CT/MRI study. *JAIDS Journal of Acquired Immune Deficiency Syndromes*, 3(5):461–471, 1990. 5

[42] Shiyu Liang, Yixuan Li, and R. Srikanth. Enhancing The Reliability of Out-of-distribution Image Detection in Neural Networks. In *6th International Conference on Learning Representations, ICLR 2018, Vancouver, BC, Canada, April 30 - May 3, 2018, Conference Track Proceedings*. OpenReview.net, 2018. 6, 8, 10, 11, 12, 13, 14, 15, 16, 17

[43] Sook-Lei Liew, Bethany P Lo, Miranda R Donnelly, Artemis Zavaliangos-Petropulu, Jessica N Jeong, Giuseppe Barisano, Alexandre Hutton, Julia P Simon, Julia M Juliano, Anisha Suri, et al. A large, curated, open-source stroke neuroimaging dataset to improve lesion segmentation algorithms. *Scientific data*, 9(1):320, 2022. 2, 5, 3

[44] Litian Liu and Yao Qin. Fast Decision Boundary based Out-of-Distribution Detector. In *Forty-first International Conference on Machine Learning, ICML 2024, Vienna, Austria, July 21-27, 2024*. OpenReview.net, 2024. 6, 9, 10, 11, 12, 13, 14, 15, 16, 17

[45] Weitang Liu, Xiaoyun Wang, John D. Owens, and Yixuan Li. Energy-based Out-of-distribution Detection. In *Advances in Neural Information Processing Systems 33: Annual Conference on Neural Information Processing Systems 2020, NeurIPS 2020, December 6-12, 2020, virtual*, 2020. 6, 7, 8, 10, 11, 12, 13, 14, 15, 16, 17

[46] Xixi Liu, Yaroslava Lochman, and Christopher Zach. GEN: Pushing the Limits of Softmax-Based Out-of-Distribution Detection. In *IEEE/CVF Conference on Computer Vision and Pattern Recognition, CVPR 2023, Vancouver, BC, Canada, June 17-24, 2023*, pages 23946–23955. IEEE, 2023. 6, 8, 10, 11, 12, 13, 14, 15, 16, 17

[47] Bjoern H. Menze, András Jakab, Stefan Bauer, Jayashree Kalpathy-Cramer, Keyvan Farahani, Justin S. Kirby, Yuliya Burren, Nicole Porz, Johannes Slotboom, Roland Wiest, Levente Lanczi, Elizabeth R. Gerstner, Marc-André Weber, Tal Arbel, Brian B. Avants, Nicholas Ayache, Patricia Buendia, D. Louis Collins, Nicolas Cordier, Jason J. Corso, Antonio Criminisi, Tilak Das, Herve Delingette, Çagatay Demiralp, Christopher R. Durst, Michel Dojat, Senan Doyle, Joana Festa, Florence Forbes, Ezequiel Geremia, Ben Glocker, Polina Golland, Xiaotao Guo, Andac Hamamci, Khan M. Iftekharuddin, Raj Jena, Nigel M. John, Ender Konukoglu, Danial Lashkari, José Antonio Mariz, Raphael Meier, Sérgio Pereira, Doina Precup, Stephen J. Price, Tammy Riklin Raviv, Syed M. S. Reza, Michael T. Ryan, Duygu Sarikaya, Lawrence H. Schwartz, Hoo-Chang Shin, Jamie Shotton, Carlos A. Silva, Nuno J. Sousa, Nagesh K. Subbanna, Gábor Székely, Thomas J. Taylor, Owen M. Thomas, Nicholas J. Tustison, Gözde B. Ünal, Flor Vasseur, Max Wintermark, Dong Hye Ye, Liang Zhao, Binsheng Zhao, Darko Zikic, Marcel Prastawa, Mauricio Reyes, and Koen Van Leemput. The Multimodal Brain Tumor Image Segmentation Benchmark (BRATS). *IEEE Trans. Medical Imaging*, 34(10):1993–2024, 2015. 2, 5, 3

[48] Samuel G. Müller and Frank Hutter. Trivialaugment: Tuning-free Yet State-of-the-Art Data Augmentation. In *2021 IEEE/CVF International Conference on Computer Vision, ICCV 2021, Montreal, QC, Canada, October 10-17, 2021*, pages 754–762. IEEE, 2021. 5

[49] Jaewoo Park, Yoon Gyo Jung, and Andrew Beng Jin Teoh. Nearest Neighbor Guidance for Out-of-Distribution Detection. In *IEEE/CVF International Conference on Computer Vision, ICCV 2023, Paris, France, October 1-6, 2023*, pages 1686–1695. IEEE, 2023. 6, 9, 10, 11, 12, 13, 14, 15, 16, 17

[50] Konstantin Pogorelov, Kristin Ranheim Randel, Carsten Grivodz, Sigrun Losada Eskeland, Thomas de Lange, Dag Johansen, Concetto Spampinato, Duc-Tien Dang-Nguyen, Mathias Lux, Peter Thelin Schmidt, et al. Kvasir: A multi-class image dataset for computer aided gastrointestinal disease detection. In *Proceedings of the 8th ACM on Multimedia Systems Conference*, pages 164–169, 2017. 2

[51] Benjamin Recht, Rebecca Roelofs, Ludwig Schmidt, and Vaishaal Shankar. Do ImageNet Classifiers Generalize to ImageNet? In *Proceedings of the 36th International Conference on Machine Learning, ICML 2019, 9-15 June 2019, Long Beach, California, USA*, pages 5389–5400. PMLR, 2019. 16, 17

[52] Jie Ren, Stanislav Fort, Jeremiah Liu, Abhijit Guha Roy, Shreyas Padhy, and Balaji Lakshminarayanan. A Simple Fix to Mahalanobis Distance for Improving Near-OOD Detection. *ArXiv preprint*, abs/2106.09022, 2021. 6, 8, 10, 11, 12, 13, 14, 15, 16, 17

[53] Tobias Rueckert. PhaKIR-Challenge at MICCAI 2024. <https://phakir.re-mic.de/>, 2024. Accessed: 2024-10-13. 2, 4, 1

[54] Tobias Rueckert, Maximilian Rieder, David Rauber, Michel Xiao, Eg Humolli, Hubertus Feussner, Dirk Wilhelm, and Christoph Palm. Augmenting instrument segmentation in video sequences of minimally invasive surgery by synthetic smoky frames. In *International Journal of Computer Assisted Radiology and Surgery*, pages S54 – S56, 2023. 4, 1

[55] Amartya Ranjan Saikia, Kangkana Bora, Lipi B Mahanta, and Anup Kumar Das. Comparative assessment of CNN architectures for classification of breast FNAC images. *Tissue and Cell*, 57:8–14, 2019. 2, 4, 1

[56] Amber L Simpson, Michela Antonelli, Spyridon Bakas, Michel Bilello, Keyvan Farahani, Bram Van Ginneken, Annette Kopp-Schneider, Bennett A Landman, Geert Litjens, Bjoern Menze, et al. A large annotated medical image dataset for the development and evaluation of segmentation algorithms. *ArXiv preprint*, abs/1902.09063, 2019. 5

[57] Leslie N Smith and Nicholay Topin. Super-convergence: Very fast training of neural networks using large learning rates. In *Artificial intelligence and machine learning*

for multi-domain operations applications, pages 369–386. SPIE, 2019. 5

[58] Yue Song, Nicu Sebe, and Wei Wang. RankFeat: Rank-1 Feature Removal for Out-of-distribution Detection. In *Advances in Neural Information Processing Systems 35: Annual Conference on Neural Information Processing Systems 2022, NeurIPS 2022, New Orleans, LA, USA, November 28 - December 9, 2022, 2022*. 6, 9, 10, 11, 12, 13, 14, 15, 16, 17

[59] Yiyou Sun and Yixuan Li. DICE: Leveraging Sparsification for Out-of-Distribution Detection. In *Computer Vision - ECCV 2022: 17th European Conference, Tel Aviv, Israel, October 23-27, 2022, Proceedings, Part XXIV*, pages 691–708. Springer, 2022. 6, 9, 10, 11, 12, 13, 14, 15, 16, 17

[60] Yiyou Sun, Chuan Guo, and Yixuan Li. ReAct: Out-of-distribution Detection With Rectified Activations. In *Advances in Neural Information Processing Systems 34: Annual Conference on Neural Information Processing Systems 2021, NeurIPS 2021, December 6-14, 2021, virtual*, pages 144–157, 2021. 6, 9, 10, 11, 12, 13, 14, 15, 16, 17

[61] Yiyou Sun, Yifei Ming, Xiaojin Zhu, and Yixuan Li. Out-of-Distribution Detection with Deep Nearest Neighbors. In *International Conference on Machine Learning, ICML 2022, 17-23 July 2022, Baltimore, Maryland, USA*, pages 20827–20840. PMLR, 2022. 6, 8, 10, 11, 12, 13, 14, 15, 16, 17

[62] Mukund Sundararajan, Ankur Taly, and Qiqi Yan. Axiomatic Attribution for Deep Networks. In *Proceedings of the 34th International Conference on Machine Learning, ICML 2017, Sydney, NSW, Australia, 6-11 August 2017*, pages 3319–3328. PMLR, 2017. 6

[63] Ilya Sutskever, James Martens, George E. Dahl, and Geoffrey E. Hinton. On the importance of initialization and momentum in deep learning. In *Proceedings of the 30th International Conference on Machine Learning, ICML 2013, Atlanta, GA, USA, 16-21 June 2013*, pages 1139–1147. JMLR.org, 2013. 5

[64] Catalina Tobon-Gomez, Arjan J. Geers, Jochen Peters, Jürgen Weese, Karen Pinto, Rashed Karim, Mohammed Ammar, Abdelaziz Daoudi, Ján Margeta, Zulma L. Sandoval, Birgit Stender, Yefeng Zheng, Maria A. Zuluaga, Julián Betancur, Nicholas Ayache, Mohammed Amine Chikh, Jean-Louis Dillenseger, B. Michael Kelm, Saïd Mahmoudi, Sébastien Ourselin, Alexander Schlaefer, Tobias Schaeffter, Reza Razavi, and Kawal S. Rhode. Benchmark for Algorithms Segmenting the Left Atrium From 3D CT and MRI Datasets. *IEEE Trans. Medical Imaging*, 34(7):1460–1473, 2015. 2, 5, 3

[65] Du Tran, Heng Wang, Lorenzo Torresani, Jamie Ray, Yann LeCun, and Manohar Paluri. A Closer Look at Spatiotemporal Convolutions for Action Recognition. In *2018 IEEE Conference on Computer Vision and Pattern Recognition, CVPR 2018, Salt Lake City, UT, USA, June 18-22, 2018*, pages 6450–6459. IEEE Computer Society, 2018. 5

[66] Andru Putra Twinanda, Sherif Shehata, Didier Mutter, Jacques Marescaux, Michel de Mathelin, and Nicolas Padoy. Endonet: A Deep Architecture for Recognition Tasks on Laparoscopic Videos. *IEEE Trans. Medical Imaging*, 36(1):86–97, 2017. 2, 4

[67] Laurens Van der Maaten and Geoffrey Hinton. Visualizing data using t-SNE. *Journal of machine learning research*, 9(11), 2008. 6

[68] Anton Vasiliuk, Daria Frolova, Mikhail Belyaev, and Boris Shirokikh. Limitations of Out-of-Distribution Detection in 3D Medical Image Segmentation. *Journal of Imaging*, 9(9):191, 2023. 2, 3, 7

[69] Sagar Vaze, Kai Han, Andrea Vedaldi, and Andrew Zisserman. Open-Set Recognition: A Good Closed-Set Classifier is All You Need. In *The Tenth International Conference on Learning Representations, ICLR 2022, Virtual Event, April 25-29, 2022*. OpenReview.net, 2022. 16, 17

[70] Haoqi Wang, Zhizhong Li, Litong Feng, and Wayne Zhang. ViM: Out-Of-Distribution with Virtual-logit Matching. In *IEEE/CVF Conference on Computer Vision and Pattern Recognition, CVPR 2022, New Orleans, LA, USA, June 18-24, 2022*, pages 4911–4920. IEEE, 2022. 6, 7, 8, 9, 10, 11, 12, 13, 14, 15, 16, 17

[71] Kai Xu, Rongyu Chen, Gianni Franchi, and Angela Yao. Scaling for Training Time and Post-hoc Out-of-distribution Detection Enhancement. In *The Twelfth International Conference on Learning Representations, ICLR 2024, Vienna, Austria, May 7-11, 2024*. OpenReview.net, 2024. 6, 9, 10, 11, 12, 13, 14, 15, 16, 17

[72] Jingkang Yang, Pengyun Wang, Dejian Zou, Zitang Zhou, Kunyuan Ding, Wenxuan Peng, Haoqi Wang, Guangyao Chen, Bo Li, Yiyou Sun, Xuefeng Du, Kaiyang Zhou, Wayne Zhang, Dan Hendrycks, Yixuan Li, and Ziwei Liu. OpenOOD: Benchmarking Generalized Out-of-Distribution Detection. In *Advances in Neural Information Processing Systems 35: Annual Conference on Neural Information Processing Systems 2022, NeurIPS 2022, New Orleans, LA, USA, November 28 - December 9, 2022*. 1, 2, 3, 5, 6, 8, 7

[73] Jingkang Yang, Kaiyang Zhou, and Ziwei Liu. Full-Spectrum Out-of-Distribution Detection. *International Journal of Computer Vision*, 131(10):2607–2622, 2023. 1, 6

[74] Jingkang Yang, Kaiyang Zhou, Yixuan Li, and Ziwei Liu. Generalized Out-of-Distribution Detection: A Survey. *International Journal of Computer Vision*, pages 1–28, 2024. 1, 3

[75] Matthew D. Zeiler and Rob Fergus. Visualizing and Understanding Convolutional Networks. In *Computer Vision - ECCV 2014 - 13th European Conference, Zurich, Switzerland, September 6-12, 2014, Proceedings, Part I*, pages 818–833. Springer, 2014. 7

[76] Jinsong Zhang, Qiang Fu, Xu Chen, Lun Du, Zelin Li, Gang Wang, Xiaoguang Liu, Shi Han, and Dongmei Zhang. Out-of-Distribution Detection based on In-Distribution Data Patterns Memorization with Modern Hopfield Energy. In *The Eleventh International Conference on Learning Representations, ICLR 2023, Kigali, Rwanda, May 1-5, 2023*. OpenReview.net, 2023. 6, 8, 10, 11, 12, 13, 14, 15, 16, 17

[77] Jingyang Zhang, Jingkang Yang, Pengyun Wang, Haoqi Wang, Yueqian Lin, Haoran Zhang, Yiyou Sun, Xuefeng Du, Kaiyang Zhou, Wayne Zhang, Yixuan Li, Ziwei Liu, Yiran Chen, and Hai Li. OpenOOD v1.5: Enhanced Benchmark

for Out-of-Distribution Detection. In *NeurIPS 2023 Workshop on Distribution Shifts: New Frontiers with Foundation Models*, 2024. 1, 2, 3, 5, 6, 7, 9

[78] Wen-zhen Zhu, Jian-pin Qi, Chuan-jia Zhan, Hong-ge Shu, Lin Zhang, Cheng-yuan Wang, Li-ming Xia, Jun-wu Hu, and Ding-yi Feng. Magnetic resonance susceptibility weighted imaging in detecting intracranial calcification and hemorrhage. *Chinese medical journal*, 121(20):2020–2025, 2008. 5

[79] David Zimmerer, Peter M. Full, Fabian Isensee, Paul Jäger, Tim Adler, Jens Petersen, Gregor Köhler, Tobias Roß, Anika Reinke, Antanas Kascenas, Bjørn Sand Jensen, Alison Q. O’Neil, Jeremy Tan, Benjamin Hou, James Batten, Huaqi Qiu, Bernhard Kainz, Nina Shvetsova, Irina Fedulova, Dmitry V. Dylov, Baolun Yu, Jianyang Zhai, Jingtao Hu, Runxuan Si, Sihang Zhou, Siqi Wang, Xinyang Li, Xuerun Chen, Yang Zhao, Sergio Naval Marimont, Giacomo Tarroni, Victor Saase, Lena Maier-Hein, and Klaus H. Maier-Hein. MOOD 2020: A Public Benchmark for Out-of-Distribution Detection and Localization on Medical Images. *IEEE Trans. Medical Imaging*, 41(10):2728–2738, 2022. 2

# OpenMIBOOD: Open Medical Imaging Benchmarks for Out-Of-Distribution Detection

## Supplementary Material

### A. Datasets

This section provides a detailed overview of all datasets used in this work. To facilitate reproducibility, we include preprocessing scripts for each dataset in our public GitHub repository, enabling the transformation of the downloaded datasets into the utilized ID and OOD datasets. For clarity, the fundamental steps executed by these scripts are outlined below.

#### A.1. MIDOG benchmark

**MIDOG** [5] The MIDOG dataset consists of 503 whole slide images stained with Hematoxylin & Eosin, a widely used stain for differentiating tissue components and evaluating tissue morphology. The dataset is divided into ten distinct domains, labeled as  $1_a$ ,  $1_b$ ,  $1_c$ ,  $2$ ,  $3$ ,  $4$ ,  $5$ ,  $6_a$ ,  $6_b$ , and  $7$ . Annotations are provided for mitotic cells and imposter cells. The preprocessing steps outlined in Sec. 3.1 yielded 451 mitotic cell crops, 724 imposter cell crops, and 1153 additional crops extracted from 50 whole slide images within the ID domain  $1_a$ . Each domain’s number corresponds to a semantic cell type shift, stemming from seven different cancer types and two species: human and canine. The cancer types include breast carcinoma, lung carcinoma, lymphosarcoma, cutaneous mast cell tumor, neuroendocrine tumor, soft tissue sarcoma, and melanoma. Furthermore, the domains display differing levels of covariate shift caused by variations in imaging hardware and staining protocols. Subscripts are used to indicate domains with multiple sources of covariate shift. Domains  $2$ ,  $3$ ,  $4$ ,  $6_a$ , and  $6_b$  exhibit covariate shifts, whereas domains  $5$  and  $7$  do not show apparent covariate shifts, as their images were generated using the same imaging hardware as the ID dataset and originate from the same institute, employing the same staining protocol as the ID set. The whole MIDOG dataset serves as ID ( $1_a$ ), cs-ID ( $1_b$ ,  $1_c$ ), and near-OOD ( $2$  –  $7$ ) datasets.

**CCAgT** [2, 4] The CCAgT dataset comprises 15 tissue slides stained using the AgNOR technique, labeled alphabetically from ‘A’ to ‘O’. The AgNOR stain specifically targets regions within the cell nucleus, providing insights into distinct cellular properties. Nuclei annotations are available for these slides and were used to generate the same type of image crops as those from the various domains of the ID dataset (Sec. 3.1). This process produced 29 675 crops which are utilized as the first far-OOD dataset.

**FNAC 2019** [55] The FNAC 2019 dataset comprises 212 images of human breast tissue samples obtained via fine needle aspiration cytology. Of these, 113 images are classified as malignant, while 99 are labeled as benign. Due to the absence of cell-level annotations, we extract cell crops through a multi-step processing pipeline. First, each image is segmented using a binary threshold with a value of 100. Next, morphological opening with a kernel size of 5 and erosion with a kernel size of 3 are applied to isolate cell clusters. From the resulting processed images, the ten largest clusters are identified, and  $50 \times 50$  px crops are generated around the centroids of these clusters. The resulting 2088 crops are subsequently utilized as the second far-OOD dataset.

#### A.2. PhaKIR benchmark

**Acknowledgements** We thank the creators of the PhaKIR dataset for granting permission to use their dataset ahead of the challenge results’ publication.

**PhaKIR** [53] The PhaKIR dataset consists of eight endoscopic videos of cholecystectomy procedures, with annotations for 19 instrument classes provided as segmentation masks and keypoints for every 25th frame. For this study, only frames containing a single surgical instrument were selected. However, one instrument class, the trocar, is exclusively an access instrument and, therefore, frequently visible alongside other surgical instruments. Consequently, frames showing a trocar in conjunction with a single surgical instrument were also included and assigned the label of the accompanying surgical instrument.

To enhance the object-to-background ratio in the selected frames, frames were excluded if the instrument covered less than 0.5% of the image area or if the distance between the instrument’s endpoint and tip was less than 150 px. In the PhaKIR dataset, the tip refers to the part of the instrument that directly contacts the organ, while the endpoint denotes the location where the instrument appears at the image border. Rueckert *et al.* [54] provided annotations for the first four videos of the PhaKIR-Challenge dataset. In this work, we extend these annotations to include Video 05 and Video 07. Following the previously established filtering process, each frame was categorized into three levels of smoke intensity by utilizing the respective annotations – none, medium, and heavy – using the corresponding annotations. The categorization criteria were as follows: None, if no smoke was perceptible; Medium, if

Table 2. Summary of available frames for each instrument class. Video 06 is employed as test data for the official challenge evaluation and therefore not publicly available.

	Video 01	Video 02	Video 03	Video 04	Video 05	Video 07	Sum
Clip-Applicator	63	151	53	22	26	0	315
Grasper	40	13	7	81	52	125	318
PE-Forceps	68	891	72	109	52	42	1234
Needle-Probe	20	27	6	29	12	31	125
Palpation-Probe	18	45	35	187	25	110	420
Suction-Rod	20	96	7	45	37	152	357
No-Instrument	198	483	323	442	166	279	1891

smoke was present but the instrument remained clearly distinguishable; and Heavy, if the instrument was no longer clearly distinguishable. Frames without visible smoke from the first six videos were designated as ID data, while frames containing medium or heavy smoke were used as cs-ID data.

Within the ID dataset, instrument classes with fewer than 80 available training images were excluded, resulting in a final dataset of 2769 frames across six instrument classes (Tab. 2). To prevent an unintended semantic shift, images from excluded instrument classes were also removed from the cs-ID sets.

**Cholec80** [66] The Cholec80 dataset comprises 80 endoscopic videos of cholecystectomies, with annotations identifying instrument classes present in every 25th frame. Consistent with the methodology used for PhaKIR, only frames containing a single surgical instrument were selected for analysis.

This dataset’s role within the MIB is to evaluate semantic shifts arising from variations in surgical instruments. Consequently, instrument classes that overlap with those in PhaKIR were excluded, yielding a total of 74 049 frames.

Most videos, except for videos 40, 60, 65, and 80, exhibit a pronounced black vignette. To avoid introducing unintended covariate shifts, a rectangular region within the vignette was cropped while maintaining the original aspect ratio of the ID images. The dataset is employed as a near-OOD dataset.

**EndoSeg15** [10] The EndoSeg15 dataset from the EndoVis 2015 challenge comprises 160 training images, evenly distributed across four distinct laparoscopic surgeries. Similar to the Cholec80 dataset, the frames in EndoSeg15 often contain black vignettes or borders, which we exclude by extracting rectangular crops with the same aspect ratio as the ID dataset. This crop is carefully positioned within the vignette or usable image content, ensuring the exclusion of black borders. The resulting dataset is then used as a near-OOD dataset.

**EndoSeg18** [1] The EndoSeg18 test dataset, part of the EndoVis Challenge 2018, consists of 1000 frames captured during four porcine surgical procedures featuring robotic instruments. No preprocessing was applied to this dataset and it was utilized for near-OOD detection evaluation.

**Kvasir-SEG** [31] The Kvasir-SEG dataset, an extension of the original Kvasir dataset introduced by Pogorelov *et al.* [50], comprises 1000 images of colorectal polyps, from which ten contain surgical instruments different from those in the ID dataset. Kvasir-SEG is employed as a far-OOD dataset.

**CATARACTS** [20] The CATARACTS dataset comprises videos of cataract surgeries and includes 21 ophthalmological instruments, which are completely distinct from those in the ID dataset. Given the large size of this dataset, we limit our analysis to the first five videos from the official test split. The initial 43, 203, 130, 29, and 159 frames were excluded from these videos, because these frames contain only black content. Afterwards, the dataset still contains 181 986 usable frames. CATARACTS is utilized as the second far-OOD dataset.

### A.3. OASIS-3 benchmark

**Acknowledgements** Data were provided in part by OASIS-3: Longitudinal Multimodal Neuroimaging: Principal Investigators: T. Benzinger, D. Marcus, J. Morris; NIH P30 AG066444, P50 AG00561, P30 NS09857781, P01 AG026276, P01 AG003991, R01 AG043434, UL1 TR000448, R01 EB009352. AV-45 doses were provided by Avid Radiopharmaceuticals, a wholly owned subsidiary of Eli Lilly.

**OASIS-3** [38] The longitudinal OASIS-3 dataset comprises 2842 MRI scans from 1378 subjects, covering multiple modalities, including T1w and T2w scans. Each scan is labeled with the number of days since the subject’s initial visit. Additionally, clinical diagnoses, also timestamped by

days since the initial visit, are provided. However, these timestamps do not precisely align between the clinical diagnoses and MRI scans, requiring the matching of clinical diagnoses to imaging visits as described in Section 3.1.

We categorize the dataset into subjects with clinical diagnoses of cognitively normal (CN) and Alzheimer’s disease (AD), using the provided diagnostic labels. Subject 30753 was excluded due to the absence of a diagnosis, and subjects 30937 and 31357 were discarded as they lacked MRI scans. Additionally, MRI scans for which the skull-stripping process failed were excluded. Specifically, this affected T2w scans from subjects 30649, 30724, and 30815, as well as a T1w scan from subject 30339.

In cases where multiple MRI scans were available for a single acquisition timestamp, the scan with the highest index number was selected. MRI scans containing only the hippocampal region were excluded to avoid introducing an unintended domain shift.

For each MRI scan, we reviewed the associated metadata to identify the acquisition device used. One out of eight scanners, namely the *Siemens Vision* device, exhibited a unique orientation and axis configuration that differed from other devices. To ensure consistency with the default orientation of the broader dataset and prevent an unintended domain shift, these images were realigned to match the orientation used by other devices.

T1w MRI scans from all devices, except the Siemens Vision, are designated as ID data. The corresponding T2w MRI scans from these subjects, if available, are labeled as cs-ID data, due to the change in imaging modality. The withheld T1w MRI scans from the Siemens Vision device are labeled as cs-ID, as the covariate shift arises from differences in the acquisition device.

Following these preprocessing steps, the final dataset consists of 944 CN and 288 AD MRI scans, forming the ID dataset.

**ATLAS** [43] The ATLAS challenge dataset consists of 33 cohorts, each containing multiple subjects with brain lesions resulting from strokes. For this study, we exclusively utilize the T1w MRI scans from the official training split. Cohorts R027, R047, R049, and R050 were excluded from our analysis due to significant quality degradation compared to the remaining cohorts. Consequently, a total of 595 MRI scans were included in the analysis as the first near-OOD dataset.

All selected OASIS-3 and ATLAS MRI scans are preprocessed by resampling to an isotropic voxel spacing of  $1\text{ mm}^3$  and applying skull-stripping using HD-BET [29], version 2.0.1 (official release).

**BraTS** [6, 7, 47] The BraTS 2023 Glioma challenge dataset includes subjects with large gliomas in the brain.

As the data was preprocessed prior to release, including steps such as resampling and skull-stripping, no further preprocessing was necessary. Therefore, the complete official training split, comprising 1251 T1w MRI scans, was used as the second near-OOD dataset.

**CT from OASIS-3** [38] In addition to the MRI data, the OASIS-3 dataset includes 1472 low-dose CT scans, which were acquired to perform attenuation correction for PET scans [38]. To emphasize brain tissue, we clipped these scans to a range of 0–80 Hounsfield units and subsequently normalized them. The resulting dataset was used as the third near-OOD dataset.

**MSD-H** [3, 64] The MSD-H dataset consists of 30 MRI scans of the human heart, all acquired during a single cardiac phase using a 3D balanced steady-state free precession acquisition method. These scans were initially employed in a benchmark for left atrium segmentation [64]. The dataset encompasses images of varying quality, ranging from high-resolution scans to those with substantial noise. Utilized as the first far-OOD dataset.

**CHAOS** [32, 33] The official test split of the CHAOS challenge dataset consists of 20 MRI scans of the abdomen, originally designed for the task of segmenting abdominal organs. The dataset includes both in-phase and out-of-phase images from dual-echo MRI sequences. For the far-OOD evaluation, we use the in-phase scans, as they exhibit stronger visual alignment with the imaging characteristics of the ID dataset, while still maintaining significant anatomical differences.

#### A.4. Splits

**MIDOG** The following randomly selected whole-slide image identifiers from MIDOG’s ID domain 1<sub>a</sub> were utilized for each respective split:

**Train:** 1, 2, 4, 5, 6, 7, 8, 9, 10, 11, 12, 13, 14, 15, 16, 18, 19, 21, 22, 23, 24, 28, 29, 30, 34, 35, 36, 37, 38, 39, 40, 41, 42, 43, 44, 45, 46, 47, 48, 50

**Validation:** 20, 26, 31, 32, 33

**Test:** 3, 17, 25, 27, 49

The remaining splits of the MIDOG dataset are detailed in Tab. 3. For the CCAgT dataset, the 15 available slides were randomly divided into three validation slides and twelve test slides, corresponding to a 20–80 split.

**Validation:** E, L, O

**Test:** A, B, C, D, F, G, H, I, J, K, M, N

The FNAC 2019 dataset comprises images categorized as either benign or malignant, and we partitioned each category separately into 10 % validation and 90 % test subsets, resulting in:

**Validation:** Benign 90–99; Malignant 103–113

Table 3. Whole slide image identifiers utilized for test and validation. 1–7 denote the different domains of the MIDOG dataset. The last row describes the total number of extracted crops per domain.

	1 <sub>b</sub>	1 <sub>c</sub>	2	3	4	5	6 <sub>a</sub>	6 <sub>b</sub>	7
<b>Test</b>	51–95	101–145	200–240	245–294	300–344	350–399	405–481	490–503	505–549
<b>Valid.</b>	96–100	145–150	241–244	295–299	345–349	400–404	482–489	504	550–553
# Crops	3258	3174	3548	16059	7202	4743	6260	974	4084

**Test:** Benign 1–89; Malignant 1–102

**PhaKIR** From the six available ID videos, one was randomly selected for validation and another for testing.

**Train:** Video 02, 03, 04, 07

**Validation:** Video 05

**Test:** Video 01

Similarly to the ID split, we use Video 05 as the validation data for the cs-ID datasets Medium Smoke and Heavy Smoke, while the remaining five videos serve as the test datasets. For the Cholec80 dataset, we employ a 10–90 split, resulting in:

**Validation:** Videos 73–80

**Test:** Videos 1–72

For EndoSeg15 and EndoSeg18, the first three videos of each dataset are designated as test data, while the remaining one is used for validation. Similarly, in the CATARACTS dataset, the first four videos are allocated as test data, with the final video serving as validation data.

For the Kvasir-SEG dataset, a 10–90 validation–test split is applied. Given the dataset’s size and the use of file-names resembling globally unique identifiers (GUIDs) individual images, it is impractical to list the exact split. Therefore, detailed information about the data split can be found in the accompanying public GitHub repository.

**OASIS-3** After preprocessing all T1w and T2w MRI scans as outlined in Appendix A.3, the remaining CN and AD data were randomly divided into 70 % for training, 15 % for validation, and 15 % for testing. For the cs-ID datasets Modality and Scanner, a randomized 10–90 split was applied for validation and test sets.

The ATLAS dataset was partitioned by assigning 10 % of the MRI scans from each cohort to the validation set, with the remaining 90 % allocated to the test set. For the MSD-H dataset, instead of performing a random split, the official test split was utilized as validation data, while the official training split was used as test data.

For the other benchmark datasets, specifically BraTS, CT data from OASIS-3, and CHAOS, the data were randomly divided into 10 % for validation and 90 % for testing.

Detailed information on the dataset sizes and specific splits can be found in the associated public GitHub repos-

Table 4. Table showing the number of ID test samples relative to the average number of cs-ID and OOD samples. The red number indicates the factor by which the average number of cs-ID and OOD samples exceeds that of the ID set.

Data source	MIDOG	PhaKIR	OASIS-3
ID test	251	427	181
cs-ID & OOD	6110 $\times$ 24.34	25 350 $\times$ 59.36	595 $\times$ 3.29

itory, which includes the exact subject identifiers and file-names for each partition.

## A.5. Metrics

In this work, we employ the AUPR<sub>IN</sub> and AUPR<sub>OUT</sub> metrics to assess OOD detection performance. However, interpreting these metrics can be challenging due to significant imbalances between ID and OOD data, which are inherent to many OOD detection tasks. Specifically, the number of OOD samples often greatly exceeds the number of ID samples, as shown in Tab. 4. This imbalance directly influences precision, defined as  $\frac{TP}{TP+FP}$ . A higher number of OOD samples increases the likelihood of false positives, leading to lower AUPR<sub>IN</sub> values due to reduced precision for ID samples. Conversely, AUPR<sub>OUT</sub> values are generally higher because the abundance of OOD samples skews precision favorably when OOD is treated as the positive class. Recall, defined as  $\frac{TP}{TP+FN}$ , is similarly affected by these imbalances.

This effect is particularly evident in the results from the Cholec80 and CATARACTS datasets within the PhaKIR benchmark, as presented in Tab. 14.

In clinical applications, however, machine learning models are more frequently exposed to ID data, where detecting rare occurrences of OOD inputs becomes crucial. Consequently, developers might prioritize highly sensitive OOD detection methods (high AUPR<sub>OUT</sub> values) to ensure such inputs are reliably flagged. At the same time, it is equally important to minimize false positive OOD detections (high AUPR<sub>IN</sub> values), as these can compromise the system’s usability. To address this trade-off, we report the harmonic mean of AUPR<sub>IN</sub> and AUPR<sub>OUT</sub> in the main text (Tab. 1),

Table 5. Metadata for the training pipeline of each MIB classifier. LR stands for learning rate, WD for weight decay, and BS for batch size.

MIB	Split	Architecture	Optimizer	Seed	Epochs	LR	WD	BS
MIDOG	80-10-10 randomly	ResNet50 [21]	SGD with $\beta$ of 0.9 [63]	0	300	$5 \times 10^{-4}$	$1 \times 10^{-1}$	128
PhaKIR	6 videos split into 4 train, 1 validation, 1 test	ResNet18 [21]	Adam [36]	0	500	$1 \times 10^{-4}$	$1 \times 10^{-3}$	48
OASIS-3	70-15-15 randomly	R(2+1)D [65]	Adam [36]	0	300	$5 \times 10^{-5}$	$1 \times 10^{-6}$	15

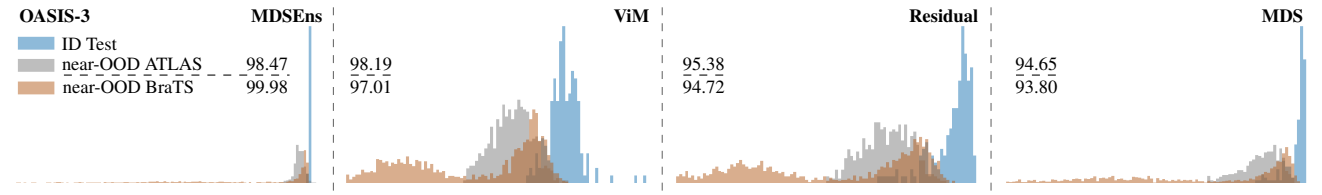


Figure 4. Distribution of OOD scores for the top four methods on two near-OOD datasets from the OASIS-3 benchmark, including AUROC values for each dataset and method.

calculated as:

$$\text{AUPR} = \frac{2 \cdot (\text{AUPR}_{\text{IN}} \cdot \text{AUPR}_{\text{OUT}})}{\text{AUPR}_{\text{IN}} + \text{AUPR}_{\text{OUT}}}$$

This approach prevents a weak performance in one metric from being overshadowed by strong results in the other, as can occur with the arithmetic mean.

By reporting a comprehensive set of metrics, including AUROC (overall OOD detection performance), FPR@95 (threshold-specific behavior), and AUPR<sub>IN</sub>/AUPR<sub>OUT</sub> (detailed insights into ID and OOD detection performance), we provide a nuanced evaluation of OOD detection performance.

## B. Experiments

### B.1. Classifier Training

Table 5 provides additional information regarding the training of each benchmark classifier. To be able to reuse existing model architectures, the final fully connected layer is replaced with a new one, where the output dimension corresponds to the number of classes in each respective classification task.

For training the MIDOG and PhaKIR classifiers, the CE loss function was weighted according to the inverse distribution of class frequencies. However, the PhaKIR training data was highly imbalanced, particularly with respect to the PE-Forceps class, which was overrepresented due to 891 images from Video 02 (Tab. 2), as well as the overall dominance of the No-Instrument class. To address this imbalance and stabilize the training process, 200 images from the PE-Forceps class in Video 02 and 400 images from all ID

training videos were randomly sampled in each epoch, with the remaining images withheld for that epoch.

A similar imbalance is present in the OASIS-3 benchmark, with 949 CN and 288 AD MRI scans in the ID data. Following the 70–15–15 split, 660 MRI and 197 MRI scans are available, respectively. To address this imbalance, 100 scans were randomly selected from the available CN and AD MRI sessions per epoch.

Table 6. The employed mean and standard deviation (SD) values for each dataset. For MIDOG and PhaKIR, the values correspond to the red, green, and blue channel.

	MIDOG	PhaKIR	OASIS-3
Mean	0.712/0.496/0.756	0.517/0.361/0.336	
SD	0.167/0.167/0.110	0.166/0.143/0.137	z-Normalization

**Augmentation** To enhance classification performance on unseen data, each classifier was trained using additional data augmentations.

For the MIDOG classifier, TrivialAugment Wide [48] was chosen, as it encompasses a diverse range of augmentations. In contrast, for the PhaKIR classifier, a custom augmentation pipeline provided the best results.

**Resize:** size=(360, 640)

**RandomHorizontalFlip:** p=0.5

**RandomPerspective:** distortion\_scale=0.2, p=0.5

**ColorJitter:** brightness=0.2, contrast=0.2, saturation=0.1, hue=0.1

Similarly, the OASIS-3 classifier was trained using a custom augmentation pipeline:

**RandomFlip:** axes='lr', p=0.5

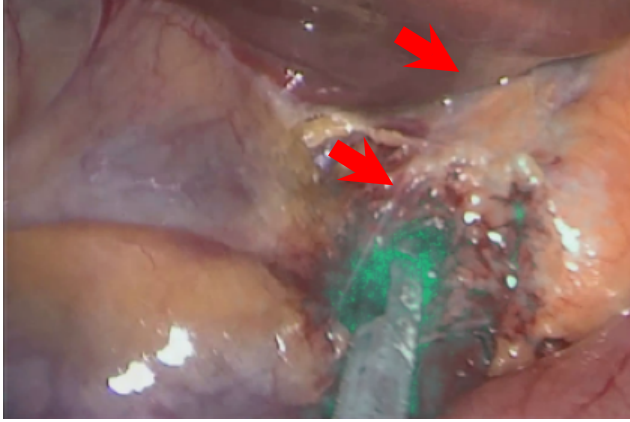


Figure 5. Image from the cs-ID Medium Smoke dataset. Classification attribution is visualized in turquoise using Integrated Gradients (Sundarajan *et al.* [62]), revealing the PhaKIR classifier’s tendency to base decisions on regions containing instruments. Arrows indicate an area with localized smoke.

**RandomAffine**: scales=(0.9, 1.1), degrees=10, isotropic=True, default\_pad\_value='minimum', p=0.9

**RandomMotion**: degrees=5, translation=5, p=0.2

**RandomNoise**: std=(0, 0.1), p=0.9

**RandomBlur**: std=(0, 0.2), p=0.9

**RandomBiasField**: coefficients=(0.1, 0.3), p=0.8

**RandomElasticDeformation**: max\_displacement=(5, 5, 5), p=0.1

The final step in each data transformation pipeline was normalization, with the corresponding values provided in Tab. 6.

## B.2. Results

The AUROC scores of the four top-performing methods on the most challenging datasets from the OASIS-3 MIB, ATLAS, and BraTS are presented in Fig. 4.

The substantial gap in discriminative power between classification- and hybrid-based methods, compared to feature-based methods, is shown in Tab. 7.

To allow for an easier interpretation of the results, Tab. 8 – Tab. 10 include descriptions for all evaluated OOD methods.

Table 7. AUROC performance averaged across all OOD detection methods for each type. The red percentages indicate the performance degradation compared to the best performing type Feature.

Information source	MIDOG	PhaKIR	OASIS-3
Feature	66.08	70.68	92.08
Combined	57.18 <span style="color:red">-13 %</span>	50.71 <span style="color:red">-28 %</span>	69.86 <span style="color:red">-24 %</span>
Classification	55.81 <span style="color:red">-16 %</span>	49.45 <span style="color:red">-30 %</span>	52.13 <span style="color:red">-43 %</span>

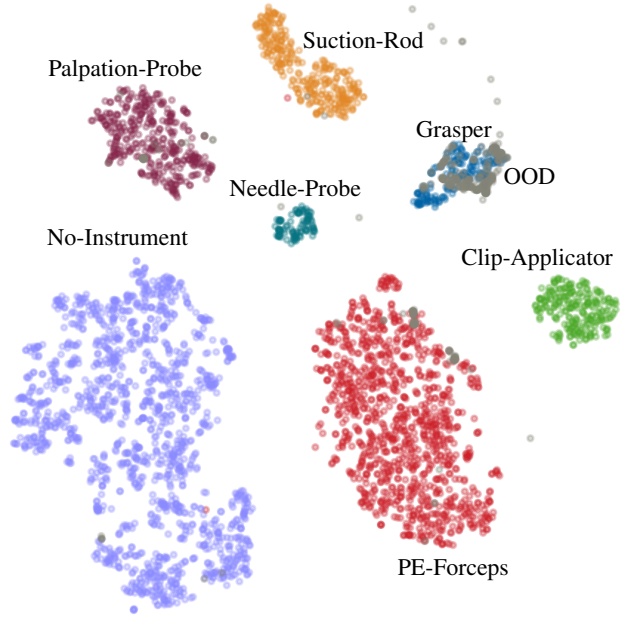


Figure 6. t-SNE [67] projection of the feature space generated by the classifier trained on the PhaKIR ID dataset. Features are from the train ID data (Class labels, colored) and the EndoSeg18 dataset (OOD, gray).

Figure 5 shows that the PhaKIR classifier predominantly bases its decisions on regions containing instruments. Thus, when smoke is located away from the instrument, it is likely that the feature embeddings are less influenced by the smoke.

In Fig. 6, the t-SNE [67] visualization of the PhaKIR classifier’s feature space illustrates that OOD samples from the EndoSeg18 dataset are primarily clustered near the Grasper class.

Figure 7 presents success and failure cases for all OOD settings. For the MIDOG and PhaKIR benchmarks, these examples are derived from the two highest-ranked methods. However, for OASIS-3, due to the lack of misclassifications in several OOD categories for MDSEns and ViM, we selected the best performing methods that still exhibit failure cases in these scenarios: SHE and RMDS.

The remaining tables in this section (Tab. 11 – Tab. 18) provide detailed results for all MIBs and their corresponding datasets across all metrics as well as for the ImageNet1k benchmark from OpenOOD [72, 73]. Entries in each table are sorted according to the overall results presented in Tab. 1.

## B.3. Employed Hyperparameters

Most OOD detection methods rely on one or more hyperparameters to optimize their performance by using the OOD validation set. The search space for each method’s param-

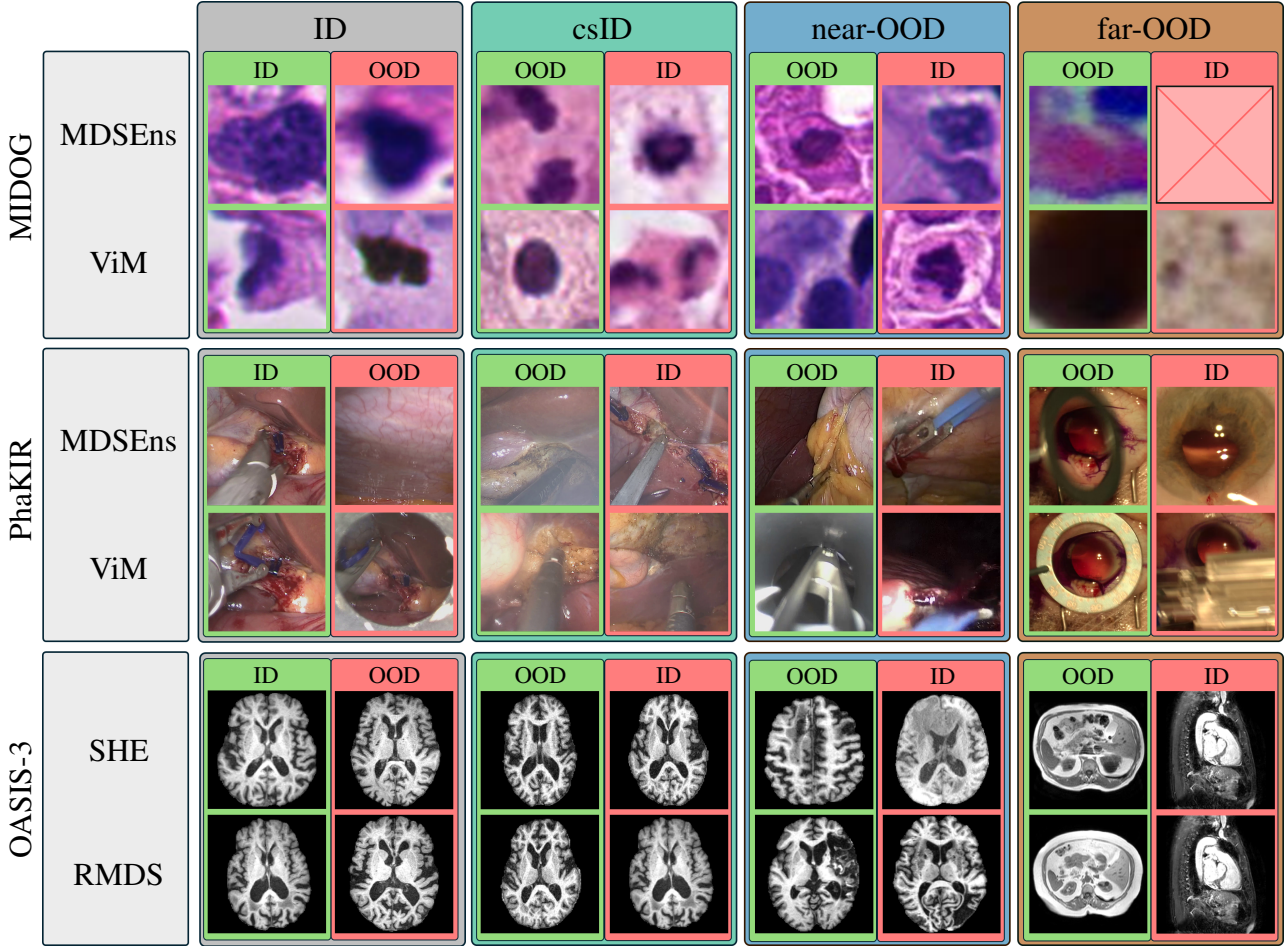


Figure 7. Example images illustrating success and failure cases across all OOD settings. We present the two top-performing methods from the MIDOG and PhaKIR benchmarks. As these methods exhibited no failure cases for several categories in the OASIS-3 benchmark, we instead selected the next two best-performing methods that exhibit failure cases: SHE and RMDS.

eters is outlined in Tab. 19. Methods not included in this table either do not have tunable hyperparameters or feature parameters that are not easily adjustable. The parameter ranges are based on the OpenOOD framework [72, 77], with minor adjustments. Table 20 provides a summary of all automatically selected hyperparameters for the OOD detection methods.

Table 8. Description of each evaluated classification-based approach.

Method	Description
EBO [45]	Motivated by energy-based learning [39], Liu <i>et al.</i> transform the final logits into a single scalar using the energy function $E(\mathbf{x}; f) = -T \cdot \log \sum_i^K e^{f_i(\mathbf{x})/T}$ . This scalar is then used as the confidence score for OOD detection.
Dropout [17]	Based on the uncertainty estimation from Gal <i>et al.</i> , this method repeatedly sets entire channels from the penultimate feature layer to zero at random. The softmax probabilities of the resulting logits' mean are used as the confidence score.
GEN [46]	Liu <i>et al.</i> take the $N$ largest softmax probability and use the generalized entropy $G_\gamma(\mathbf{p}) = \sum_i p_i^\gamma (1 - p_i)^\gamma$ as confidence score.
KLM [24]	Hendrycks <i>et al.</i> compute the class-wise distribution of mean softmax probabilities. During inference the minimal Kullback-Leibler divergence between these mean distributions and the current sample distribution is used as confidence score.
MLS [26]	Instead of employing the maximum softmax probability, Hendrycks <i>et al.</i> use the maximum logit as confidence score.
MSP [23]	As one of the earliest baselines, Hendrycks <i>et al.</i> use the maximum softmax probability as confidence score.
ODIN [42]	Liang <i>et al.</i> employ input perturbation and subsequent temperature scaling on the logits. Subsequently, the maximum softmax probability from these logits is used as confidence score.
OpenMax [8]	Bendale and Boult first estimate Weibull distributions for all classes based on the top $k$ distances to mean logits. These distributions are used to rescale the logits. Subsequently an additional pseudo-logit is added, while the total activation level remains constant, which serves as OOD class. The probability of this pseudo-class is used as confidence score.
TempScale [19]	Guo <i>et al.</i> learn a temperature scaling on the ID dataset and use the temperature-scaled softmax probabilities as confidence score.

Table 9. Description of each evaluated feature-based approach.

Method	Description
KNN [61]	Sun <i>et al.</i> compute the $k$ -th nearest neighbor of a sample inside the set of normalized activations from the penultimate layer. The distance to this neighbor is used as confidence score.
MDS [40]	Lee <i>et al.</i> uses the Mahalanobis distance between a sample's penultimate layer activations and class conditional Gaussian distributions derived from ID data.
MDSEns [40]	Lee <i>et al.</i> extend MDS by aggregating these distances from all intermediate layers through weighted averaging. Additionally, input perturbation from ODIN is applied.
Residual [70]	Wang <i>et al.</i> project the activations from the penultimate layer to a low-variance subspace defined by the $N$ smallest eigenvalues of the empirical covariance matrix, estimated from ID data and uses the norm of those activations as confidence score.
RMDS [52]	Ren <i>et al.</i> extend MDS by introducing an additional Mahalanobis distance, computed between the penultimate layer activations and the Gaussian distribution estimated from the entire ID dataset. The final confidence score is obtained by subtracting this new distance from the original MDS distances.
SHE [76]	Zhang <i>et al.</i> define confidence scores using the distance between a sample's penultimate-layer activations and its class-conditional mean, computed exclusively from correctly classified samples.

Table 10. Description of each evaluated hybrid-based approach.

Method	Description
ASH [15]	Djurisic <i>et al.</i> set the lowest $p$ th-percentile of activations in the penultimate layer to zero. The remaining activations are then processed in one of three ways: they are either left unchanged, replaced with a positive constant, or scaled by a ratio derived from the activations before and after pruning. Subsequently, these adjusted activations are used as input to the energy-score from EBO to yield the confidence score. We follow the implementation from OpenOOD [77] and use the variant with positive constants.
DICE [59]	Sun <i>et al.</i> calculate the class-wise contribution of weights in the final fully-connected layer based on the empirically estimated ID mean of the ID dataset. By preserving only the $p$ -th percentile of the most important weights, they calculate the final logits and use those as input to the energy-score from EBO to yield the confidence score.
fDBD [44]	Liu <i>et al.</i> estimate the distance of the penultimate layers' features to class-decision boundaries and regularize this distance by the distance between the activation and the mean of activations from the ID dataset.
NNGuide [49]	Park <i>et al.</i> use the average distance of a samples' activation from the penultimate layer to the ID distribution of activations and use it to scale the energy-score from EBO to yield the confidence score.
RankFeat [58]	Song <i>et al.</i> propose to remove the rank-1 matrix from activations from the two last feature layers. These matrices are composed by the largest singular value established from a Singular Value Decomposition. The adjusted activations are forwarded to yield new logits, which are then averaged and used as input to the energy-score from EBO to yield the confidence score.
ReAct [60]	Sun <i>et al.</i> calculate a threshold from the $p$ th-percentile of all ID activations in the penultimate layer and use this threshold to set activations above this threshold to zero. Subsequently, logits resulting from these activations serve as input to the energy-score from EBO, yielding the final confidence score.
Relation [35]	Kim <i>et al.</i> estimate the relational structure on the feature-space of the penultimate layer based on the activations and corresponding class labels. This structure allows to identify similar feature embeddings with different label information. The confidence score is then calculated by evaluating their proposed similarity functions on a subset of the ID data.
SCALE [71]	Motivated by ASH, Xu <i>et al.</i> omit the pruning step from ASH but keep the activation scaling based on the $p$ th-percentile of activations. These activations are then used as input to the energy-score from EBO to yield the confidence score.
ViM [70]	Wang <i>et al.</i> create an additional virtual-logit based on the subspace from Residual and calculate the energy-score over this and the original logits.

Table 11. Results from the MIDOG benchmark for the AUROC and FPR@95 metrics.

	cs-ID			near-OOD						far-OOD				
	1 <sub>b</sub>	1 <sub>c</sub>	Avg	2	3	4	5	6 <sub>a</sub>	6 <sub>b</sub>	7	Avg	CCAgT	FNAC	Avg
<b>AUROC↑</b>														
MDSEns [40]	98.56	99.82	99.19	99.56	99.71	99.68	71.50	98.95	99.71	73.78	91.84	100.00	100.00	100.00
ViM [70]	58.97	60.48	59.73	69.06	68.22	65.87	61.97	61.78	61.13	50.65	62.67	89.80	79.76	84.78
Residual [70]	57.87	62.65	60.26	72.56	72.15	67.57	64.48	65.21	63.56	54.89	65.78	94.80	89.91	92.35
MDS [40]	56.89	60.31	58.60	68.94	68.20	65.60	63.67	62.64	60.96	52.45	63.21	93.50	88.31	90.91
KNN [61]	56.72	59.21	57.97	66.62	70.41	63.45	63.25	59.22	57.82	50.62	61.63	91.10	89.26	90.18
SHE [76]	57.06	58.72	57.89	66.92	68.49	61.20	62.96	60.73	61.27	51.03	61.80	91.12	91.06	91.09
RMDS [52]	49.06	49.87	49.46	50.35	50.69	51.44	56.05	52.53	49.61	54.97	52.23	59.98	61.39	60.68
Relation [35]	54.93	56.42	55.68	62.68	62.23	59.27	62.12	58.08	56.43	50.17	58.71	86.10	86.24	86.17
fDBD [44]	50.74	54.33	52.54	60.80	58.02	58.06	61.83	59.43	54.10	56.06	58.33	82.99	83.06	83.03
SCALE [71]	51.65	55.24	53.44	55.61	58.63	54.22	59.14	53.91	53.20	55.27	55.71	79.68	84.38	82.03
ReAct [60]	51.83	55.74	53.79	58.58	59.30	56.56	61.23	56.79	52.94	56.41	57.40	83.78	85.94	84.86
ASH [15]	52.31	55.55	53.93	56.14	59.47	54.63	59.47	53.94	53.65	54.86	56.02	80.47	84.93	82.70
RankFeat [58]	48.37	47.98	48.17	48.99	51.63	52.01	56.12	52.75	41.39	59.91	51.83	64.90	47.97	56.44
OpenMax [8]	48.80	50.96	49.88	53.78	53.29	53.11	56.77	52.08	48.45	51.80	52.75	67.44	64.30	65.87
ODIN [42]	52.82	59.94	56.38	64.40	71.77	58.36	59.69	60.36	62.31	52.69	61.37	79.61	90.56	85.08
GEN [46]	51.00	54.08	52.54	56.22	58.26	55.74	59.97	53.75	50.83	53.46	55.46	77.88	81.68	79.78
MSP [23]	51.71	55.02	53.37	56.70	58.86	56.01	60.16	54.09	51.80	53.71	55.90	78.83	83.00	80.91
Dropout [17]	51.56	54.95	53.25	56.57	58.70	55.84	60.00	53.95	51.65	53.60	55.76	78.78	82.96	80.87
TempScale [19]	51.91	55.23	53.57	56.84	59.08	56.10	60.25	54.21	52.00	53.83	56.05	79.24	83.52	81.38
NNGuide [49]	56.79	59.38	58.08	61.63	68.14	58.95	61.74	56.47	58.61	53.31	59.84	87.33	91.83	89.58
KLM [24]	47.92	48.76	48.34	50.92	47.45	51.34	56.05	53.14	48.70	53.22	51.54	71.49	75.57	73.53
EBO [45]	52.70	56.21	54.46	57.34	60.33	56.08	60.90	55.00	53.33	54.97	56.85	82.02	86.88	84.45
MLS [26]	52.50	55.94	54.22	57.17	59.88	56.13	60.62	54.70	53.02	54.56	56.58	80.59	85.37	82.98
DICE [59]	49.63	53.49	51.56	53.23	52.74	53.55	59.72	53.44	49.58	56.80	54.15	76.38	81.79	79.08
<b>FPR@95↓</b>														
MDSEns [40]	3.59	0.80	2.19	1.20	1.20	1.20	84.06	1.99	1.20	86.85	25.38	0.00	0.00	0.00
ViM [70]	89.64	85.66	87.65	79.68	79.68	79.68	86.45	84.86	87.25	90.04	83.95	40.24	54.58	47.41
Residual [70]	91.24	86.45	88.84	78.09	76.89	78.88	87.65	84.06	85.66	91.24	83.21	22.71	36.25	29.48
MDS [40]	89.24	86.85	88.05	78.49	78.49	79.68	86.85	84.06	86.85	92.83	83.89	32.67	41.83	37.25
KNN [61]	86.06	90.04	88.05	82.07	73.71	85.26	90.84	94.42	89.24	97.21	87.54	29.88	39.84	34.86
SHE [76]	84.86	87.25	86.06	80.08	76.10	85.26	89.64	94.02	84.86	96.41	86.62	28.29	34.66	31.47
RMDS [52]	96.02	95.62	95.82	96.81	96.81	95.62	95.62	96.81	91.63	95.56	99.20	99.20	99.20	99.20
Relation [35]	86.45	86.85	86.65	80.88	79.28	83.67	87.25	90.44	87.25	97.21	86.57	37.05	50.20	43.63
fDBD [44]	93.63	92.83	93.23	85.66	84.06	88.05	90.04	88.05	92.03	92.03	88.56	55.78	64.14	59.96
SCALE [71]	97.21	96.81	97.01	93.23	84.86	97.21	95.22	96.81	90.44	95.22	93.28	76.49	67.73	72.11
ReAct [60]	94.42	92.83	93.63	92.83	89.64	94.82	94.42	94.82	94.82	92.83	93.45	46.22	58.17	52.19
ASH [15]	96.02	95.62	95.82	92.43	85.26	96.41	94.42	95.62	90.44	95.62	92.89	74.50	65.34	69.92
RankFeat [58]	95.62	96.81	96.22	95.62	95.22	95.22	94.02	95.22	98.01	93.23	95.22	87.25	97.21	92.23
OpenMax [8]	94.02	92.03	93.03	90.44	86.06	93.63	92.43	94.02	89.64	94.82	91.58	62.55	66.53	64.54
ODIN [42]	95.22	93.23	94.22	89.24	78.49	94.02	93.63	92.03	88.84	96.41	90.38	86.85	54.18	70.52
GEN [46]	94.42	93.63	94.02	90.84	86.85	94.82	93.23	94.82	91.24	96.02	92.54	63.35	62.55	62.95
MSP [23]	94.02	93.63	93.82	90.84	86.45	94.42	93.63	94.82	91.24	96.02	92.49	63.75	61.75	62.75
Dropout [17]	94.82	94.02	94.42	91.24	86.85	94.82	92.83	95.22	91.24	96.41	92.66	64.14	62.95	63.55
TempScale [19]	94.02	93.63	93.82	90.84	86.45	94.42	93.63	94.82	91.24	96.02	92.49	63.75	60.96	62.35
NNGuide [49]	92.83	92.43	92.63	88.05	78.49	94.02	92.03	94.82	87.65	96.81	90.27	54.58	35.46	45.02
KLM [24]	96.41	94.02	95.22	94.42	97.21	94.82	93.63	93.63	92.43	93.63	94.25	75.70	91.63	83.67
EBO [45]	94.42	94.02	94.22	91.24	86.06	94.42	92.83	94.42	91.24	96.02	92.32	67.33	58.17	62.75
MLS [26]	94.42	94.02	94.22	91.24	86.45	94.42	93.23	94.42	91.24	96.02	92.43	66.93	58.96	62.95
DICE [59]	96.02	96.02	96.02	95.62	93.23	96.02	94.02	96.02	95.22	94.02	94.88	63.75	72.51	68.13

Table 12. Results from the MIDOG benchmark for the AUPR<sub>IN</sub> and AUPR<sub>OUT</sub> metrics.

	cs-ID			near-OOD							far-OOD			
	1 <sub>b</sub>	1 <sub>c</sub>	Avg	2	3	4	5	6 <sub>a</sub>	6 <sub>b</sub>	7	Avg	CCAgT	FNAC	Avg
<b>AUPR<sub>IN</sub>↑</b>														
MDSEns [40]	95.64	99.28	97.46	98.85	98.83	98.86	13.30	97.90	99.55	13.16	74.35	100.00	99.99	100.00
ViM [70]	10.20	12.75	11.48	16.55	5.27	9.69	10.49	7.24	30.35	7.58	12.45	44.07	57.24	50.65
Residual [70]	10.35	13.69	12.02	19.55	6.85	12.35	10.88	8.92	34.45	8.00	14.43	55.84	72.06	63.95
MDS [40]	10.46	13.03	11.74	19.06	7.30	12.41	11.35	8.78	32.40	7.32	14.09	51.93	67.59	59.76
KNN [61]	11.81	11.15	11.48	15.55	11.42	9.60	10.33	6.15	31.42	6.33	12.97	28.37	65.82	47.10
SHE [76]	16.30	13.74	15.02	18.78	12.18	8.71	10.78	6.65	35.75	6.50	14.19	55.35	72.39	63.87
RMDS [52]	7.55	7.59	7.57	6.82	1.61	3.99	7.41	4.39	21.76	7.97	7.71	1.32	13.77	7.54
Relation [35]	15.31	13.28	14.29	17.75	10.19	8.70	10.96	6.70	32.53	6.50	13.33	47.93	62.33	55.13
fDBD [44]	8.45	9.15	8.80	12.10	3.50	6.35	10.03	6.96	26.48	8.41	10.55	29.44	51.14	40.29
SCALE [71]	8.48	9.06	8.77	8.81	3.12	4.39	8.62	4.63	25.63	7.82	9.00	4.27	44.60	24.44
ReAct [60]	8.54	9.41	8.98	9.24	2.80	4.89	8.98	5.07	23.87	8.60	9.06	14.11	47.90	31.00
ASH [15]	8.67	9.16	8.92	8.98	3.26	4.46	8.75	4.64	25.93	7.65	9.09	4.62	45.69	25.15
RankFeat [58]	7.34	7.17	7.26	6.83	1.71	4.14	7.65	4.42	18.55	8.49	7.40	2.08	10.66	6.37
OpenMax [8]	7.96	8.63	8.30	8.56	2.62	4.55	8.31	4.49	23.30	7.21	8.43	4.75	39.87	22.31
ODIN [42]	8.27	10.47	9.37	11.76	5.86	4.90	8.58	5.84	33.21	6.78	10.99	3.28	57.47	30.37
GEN [46]	8.78	9.26	9.02	9.50	3.61	4.80	8.98	5.03	24.56	6.99	9.07	5.65	46.10	25.88
MSP [23]	8.94	9.48	9.21	9.81	3.83	4.81	8.99	5.07	25.25	6.97	9.25	5.69	46.54	26.12
Dropout [17]	8.85	9.36	9.10	9.67	3.64	4.82	8.91	5.02	24.94	6.94	9.13	5.51	46.43	25.97
TempScale [19]	8.97	9.52	9.24	9.84	3.85	4.82	9.01	5.09	25.34	6.98	9.27	5.72	46.84	26.28
NNGuide [49]	12.98	11.51	12.24	13.28	8.84	5.83	9.73	5.09	31.69	6.62	11.58	11.56	71.19	41.38
KLM [24]	7.03	7.55	7.29	7.22	1.48	3.95	7.76	4.61	23.32	7.24	7.94	3.02	21.62	12.32
EBO [45]	9.08	9.66	9.37	9.73	3.78	4.76	9.00	5.12	25.99	7.16	9.37	5.52	49.42	27.47
MLS [26]	9.04	9.62	9.33	9.72	3.76	4.78	8.98	5.10	25.81	7.11	9.32	5.53	48.48	27.01
DICE [59]	8.02	8.54	8.28	8.24	2.49	4.44	8.90	4.91	22.98	8.36	8.62	4.94	33.88	19.41
<b>AUPR<sub>OUT</sub>↑</b>														
MDSEns [40]	99.77	99.98	99.88	99.95	99.99	99.98	97.04	99.89	99.88	97.23	99.14	100.00	100.00	100.00
ViM [70]	94.72	94.76	94.74	96.52	99.19	97.68	95.31	97.22	85.78	93.33	95.00	99.85	95.81	97.83
Residual [70]	94.43	95.20	94.82	97.06	99.32	97.89	95.91	97.59	86.93	94.44	95.59	99.93	98.19	99.06
MDS [40]	94.22	94.82	94.52	96.55	99.20	97.72	95.74	97.38	85.87	94.13	95.23	99.91	97.90	98.91
KNN [61]	93.92	94.50	94.21	95.97	99.22	97.48	95.97	97.09	83.43	94.39	94.79	99.87	98.26	99.07
SHE [76]	93.94	94.49	94.21	96.01	99.16	97.33	95.94	97.20	84.46	94.43	94.93	99.87	98.59	99.23
RMDS [52]	92.10	92.54	92.32	93.25	98.42	96.30	94.69	96.17	77.70	94.38	92.99	99.25	92.70	95.97
Relation [35]	93.36	93.88	93.62	95.22	98.92	97.07	95.67	96.86	81.93	94.17	94.26	99.76	97.66	98.71
fDBD [44]	92.92	93.81	93.36	95.22	98.83	97.07	95.66	97.00	81.85	94.76	94.34	99.73	97.25	98.49
SCALE [71]	92.76	93.69	93.23	94.29	98.78	96.73	95.45	96.57	80.31	94.83	93.85	99.68	97.57	98.62
ReAct [60]	92.89	93.86	93.37	94.82	98.85	96.91	95.70	96.83	80.88	94.95	94.13	99.75	97.86	98.80
ASH [15]	92.92	93.76	93.34	94.41	98.82	96.77	95.50	96.58	80.61	94.79	93.93	99.69	97.67	98.68
RankFeat [58]	91.52	91.64	91.58	92.42	98.32	96.16	94.44	96.07	72.45	95.41	92.18	99.16	87.55	93.35
OpenMax [8]	91.49	91.81	91.65	93.15	98.25	96.12	94.10	95.77	76.13	93.03	92.37	99.01	87.31	93.16
ODIN [42]	92.98	94.52	93.75	95.85	99.28	97.14	95.57	97.27	84.79	94.39	94.90	99.69	98.66	99.18
GEN [46]	92.47	93.22	92.84	94.12	98.70	96.72	95.23	96.37	78.93	94.28	93.48	99.56	96.08	97.82
MSP [23]	92.64	93.48	93.06	94.30	98.75	96.79	95.37	96.48	79.44	94.46	93.66	99.62	96.99	98.30
Dropout [17]	92.63	93.48	93.06	94.29	98.75	96.78	95.36	96.47	79.37	94.46	93.64	99.62	96.99	98.30
TempScale [19]	92.70	93.55	93.13	94.35	98.77	96.81	95.42	96.51	79.68	94.53	93.72	99.63	97.17	98.40
NNGuide [49]	93.77	94.44	94.11	95.31	99.14	97.18	95.89	96.89	82.89	94.79	94.58	99.82	98.78	99.30
KLM [24]	92.77	92.85	92.81	93.68	98.49	96.57	95.01	96.46	78.91	94.38	93.36	99.53	96.24	97.89
EBO [45]	92.97	93.89	93.43	94.63	98.87	96.87	95.71	96.72	80.71	94.91	94.06	99.73	98.05	98.89
MLS [26]	92.90	93.78	93.34	94.51	98.83	96.86	95.59	96.63	80.38	94.75	93.94	99.68	97.70	98.69
DICE [59]	91.68	93.04	92.36	93.39	98.36	96.33	95.39	96.31	76.77	94.94	93.07	99.57	97.13	98.35

Table 13. Results from the PhaKIR benchmark for the AUROC and FPR@95 metrics. M. Smoke and H. Smoke stands for Medium and Heavy Smoke. CAT. stands for CATARACTS.

	cs-ID			near-OOD			far-OOD			
	M. Smoke	H. Smoke	Avg	Cholec80	EndoSeg15	EndoSeg18	Avg	Kvasir	CAT.	Avg
<b>AUROC↑</b>										
MDSEns [40]	45.67	84.43	65.05	96.65	94.81	99.87	97.11	99.98	97.02	98.50
ViM [70]	63.64	81.14	72.39	68.44	83.25	91.73	81.14	50.04	60.64	55.34
Residual [70]	39.11	75.13	57.12	59.53	75.98	95.46	76.99	48.33	66.30	57.31
MDS [40]	38.25	73.84	56.04	58.27	76.37	94.81	76.48	40.20	62.75	51.47
KNN [61]	24.01	44.09	34.05	64.17	61.22	40.92	55.44	31.22	44.28	37.75
SHE [76]	25.89	46.47	36.18	62.40	55.13	33.48	50.34	54.30	40.50	47.40
RMDS [52]	31.67	44.76	38.22	60.86	69.85	72.48	67.73	24.98	45.99	35.49
Relation [35]	24.41	37.72	31.06	62.98	63.50	56.57	61.02	26.55	34.90	30.72
fDBD [44]	26.38	33.78	30.08	58.13	54.72	37.56	50.13	18.10	36.98	27.54
SCALE [71]	27.35	44.46	35.91	61.19	42.47	13.26	38.97	47.75	45.91	46.83
ReAct [60]	24.15	36.52	30.34	58.08	52.64	34.41	48.38	16.63	35.16	25.89
ASH [15]	36.95	55.04	45.99	60.14	42.62	17.76	40.17	73.39	56.78	65.08
RankFeat [58]	54.27	49.75	52.01	41.96	51.71	42.10	45.26	14.61	40.09	27.35
OpenMax [8]	23.95	39.85	31.90	64.55	69.04	64.51	66.03	31.21	35.90	33.56
ODIN [42]	31.16	37.39	34.28	63.17	43.58	18.59	41.78	83.53	60.10	71.82
GEN [46]	24.16	41.14	32.65	61.29	55.97	37.40	51.55	29.33	36.02	32.68
MSP [23]	23.77	40.30	32.04	61.67	54.20	34.61	50.16	28.45	36.56	32.51
Dropout [17]	23.78	40.13	31.96	61.41	54.27	34.60	50.10	28.59	36.52	32.56
TempScale [19]	23.56	39.90	31.73	61.73	52.96	31.49	48.73	27.87	37.12	32.50
NNGuide [49]	21.87	36.43	29.15	60.93	42.19	10.84	37.98	34.56	47.32	40.94
KLM [24]	52.39	57.91	55.15	57.33	58.25	53.45	56.34	29.09	42.64	35.87
EBO [45]	23.74	40.25	31.99	60.77	45.38	14.38	40.18	27.36	41.32	34.34
MLS [26]	23.74	40.25	32.00	60.76	45.36	14.39	40.17	27.35	41.31	34.33
DICE [59]	30.22	41.70	35.96	60.62	57.94	41.43	53.33	22.47	22.82	22.65
<b>FPR@95↓</b>										
MDSEns [40]	100.00	56.67	78.34	14.99	15.93	0.70	10.54	0.00	8.90	4.45
ViM [70]	95.78	78.69	87.24	84.54	52.22	28.34	55.04	95.08	93.21	94.15
Residual [70]	99.53	86.42	92.97	88.52	62.06	16.63	55.74	91.57	85.48	88.52
MDS [40]	99.30	84.54	91.92	89.23	64.17	18.97	57.46	94.61	84.54	89.58
KNN [61]	100.00	98.59	99.30	85.95	86.65	95.78	89.46	94.15	97.89	96.02
SHE [76]	99.77	98.13	98.95	90.40	92.74	99.06	94.07	93.21	99.06	96.14
RMDS [52]	97.89	91.10	94.50	82.90	75.18	92.97	83.68	95.55	92.97	94.26
Relation [35]	99.53	97.42	98.48	83.14	76.35	64.64	74.71	96.02	100.00	98.01
fDBD [44]	95.78	90.16	92.97	84.07	82.44	83.84	83.45	96.96	99.53	98.24
SCALE [71]	100.00	99.06	99.53	90.40	97.42	100.00	95.94	77.99	86.89	82.44
ReAct [60]	97.19	94.38	95.78	88.76	83.37	89.70	87.28	98.36	100.00	99.18
ASH [15]	99.77	93.68	96.72	85.48	94.85	100.00	93.44	52.46	73.54	63.00
RankFeat [58]	96.02	95.32	95.67	92.51	89.70	94.61	92.27	97.66	91.80	94.73
OpenMax [8]	100.00	100.00	100.00	87.59	93.44	99.30	93.44	94.85	99.30	97.07
ODIN [42]	100.00	100.00	100.00	100.00	100.00	100.00	100.00	50.12	76.81	63.47
GEN [46]	100.00	100.00	100.00	91.10	95.55	99.77	95.47	95.08	98.59	96.84
MSP [23]	100.00	100.00	100.00	90.87	96.25	100.00	95.71	94.38	98.59	96.49
Dropout [17]	100.00	100.00	100.00	90.63	96.96	100.00	95.86	94.38	98.36	96.37
TempScale [19]	100.00	100.00	100.00	90.63	96.02	100.00	95.55	94.38	98.59	96.49
NNGuide [49]	100.00	100.00	100.00	91.80	96.49	100.00	96.10	88.06	91.80	89.93
KLM [24]	86.89	88.76	87.82	96.96	76.35	61.83	78.38	93.91	95.55	94.73
EBO [45]	99.77	99.06	99.41	91.80	98.13	100.00	96.64	93.21	94.85	94.03
MLS [26]	99.77	99.06	99.41	91.80	98.13	100.00	96.64	93.21	94.85	94.03
DICE [59]	100.00	100.00	100.00	93.91	95.78	99.77	96.49	100.00	100.00	100.00

Table 14. Results from the PhaKIR benchmark for the AUPR<sub>IN</sub> and AUPR<sub>OUT</sub> metrics. M. Smoke and H. Smoke stands for Medium and Heavy Smoke. CAT. stands for CATARACTS.

	cs-ID			near-OOD			far-OOD			
	M. Smoke	H. Smoke	Avg	Cholec80	EndoSeg15	EndoSeg18	Avg	Kvasir	CAT.	Avg
<b>AUPR<sub>IN</sub>↑</b>										
MDSEns [40]	29.60	69.21	49.41	73.26	98.59	99.80	90.55	99.96	87.55	93.75
ViM [70]	40.23	61.00	50.61	2.46	94.66	89.08	62.07	31.28	0.82	16.05
Residual [70]	27.14	52.52	39.83	1.16	92.18	94.58	62.64	32.41	1.11	16.76
MDS [40]	26.85	51.74	39.29	1.10	92.31	93.55	62.32	27.96	1.02	14.49
KNN [61]	22.77	27.39	25.08	1.41	84.54	32.37	39.44	26.53	0.33	13.43
SHE [76]	23.14	29.06	26.10	0.99	80.58	27.50	36.35	36.09	0.36	18.22
RMDS [52]	25.57	34.20	29.89	1.48	88.00	54.44	47.97	24.84	0.86	12.85
Relation [35]	22.78	25.66	24.22	1.41	87.45	59.25	49.37	23.63	0.27	11.95
fDBD [44]	25.35	29.13	27.24	1.57	84.08	41.98	42.54	20.71	0.28	10.50
SCALE [71]	23.45	27.33	25.39	0.90	73.50	22.14	32.18	45.45	0.84	23.14
ReAct [60]	23.66	28.07	25.86	1.01	82.82	37.00	40.28	19.93	0.27	10.10
ASH [15]	26.14	35.08	30.61	1.05	75.74	23.02	33.27	71.80	1.31	36.55
RankFeat [58]	36.56	33.82	35.19	1.22	80.96	34.21	38.80	21.17	0.90	11.03
OpenMax [8]	22.75	25.59	24.17	1.11	84.98	40.47	42.19	26.16	0.28	13.22
ODIN [42]	34.63	34.94	34.78	12.38	78.09	33.44	41.30	77.69	12.47	45.08
GEN [46]	22.75	26.04	24.40	0.97	79.95	28.26	36.39	26.05	0.28	13.17
MSP [23]	22.67	25.79	24.23	0.96	79.29	27.31	35.86	25.80	0.29	13.04
Dropout [17]	22.66	25.76	24.21	0.96	79.27	27.33	35.85	26.00	0.29	13.14
TempScale [19]	22.62	25.66	24.14	0.95	78.64	26.30	35.30	25.72	0.30	13.01
NNGuide [49]	22.34	24.49	23.41	0.89	73.06	21.80	31.92	33.96	1.05	17.50
KLM [24]	42.03	42.02	42.02	0.76	84.61	54.99	46.79	26.08	0.35	13.21
EBO [45]	22.60	26.00	24.30	0.90	74.94	22.31	32.72	27.38	0.50	13.94
MLS [26]	22.60	26.00	24.30	0.90	74.94	22.31	32.72	27.38	0.50	13.94
DICE [59]	24.35	26.03	25.19	0.85	80.38	29.65	36.96	20.85	0.23	10.54
<b>AUPR<sub>OUT</sub>↑</b>										
MDSEns [40]	63.55	92.10	77.83	99.97	83.02	99.92	94.31	99.99	99.98	99.99
ViM [70]	79.28	90.54	84.91	99.67	56.84	93.99	83.50	72.87	99.77	86.32
Residual [70]	60.54	87.27	73.91	99.52	44.71	96.78	80.34	67.50	99.79	83.65
MDS [40]	59.45	86.08	72.76	99.49	44.72	96.38	80.20	61.44	99.76	80.60
KNN [61]	53.15	66.78	59.96	99.57	26.56	55.74	60.62	55.42	99.61	77.51
SHE [76]	54.59	68.58	61.59	99.56	23.59	52.13	58.43	70.69	99.53	85.11
RMDS [52]	54.15	60.83	57.49	99.43	32.88	78.20	70.17	52.34	99.62	75.98
Relation [35]	52.51	61.55	57.03	99.56	26.44	61.97	62.66	53.14	99.49	76.31
fDBD [44]	51.58	57.02	54.30	99.50	22.32	53.05	58.29	50.25	99.53	74.89
SCALE [71]	53.78	66.55	60.17	99.56	19.02	44.81	54.46	61.78	99.59	80.68
ReAct [60]	51.03	59.10	55.07	99.49	21.66	51.43	57.52	49.90	99.52	74.71
ASH [15]	61.16	75.83	68.50	99.54	18.66	46.01	54.74	76.77	99.66	88.21
RankFeat [58]	68.24	65.31	66.77	99.07	21.02	55.80	58.63	49.21	99.48	74.34
OpenMax [8]	52.83	62.91	57.87	99.58	37.71	82.03	73.11	58.21	99.44	78.82
ODIN [42]	55.84	66.78	61.31	99.62	19.55	42.94	54.04	88.09	99.70	93.90
GEN [46]	53.06	64.94	59.00	99.53	26.20	57.69	61.14	54.70	99.47	77.09
MSP [23]	52.19	62.79	57.49	99.55	22.94	53.90	58.80	53.92	99.49	76.71
Dropout [17]	52.14	62.57	57.35	99.55	22.96	53.77	58.76	53.93	99.49	76.71
TempScale [19]	51.98	62.57	57.28	99.56	22.32	52.01	57.96	53.68	99.50	76.59
NNGuide [49]	50.90	60.83	55.87	99.53	18.50	44.13	54.05	56.01	99.62	77.82
KLM [24]	62.48	70.24	66.36	99.49	23.76	60.34	61.19	54.04	99.54	76.79
EBO [45]	51.59	62.26	56.93	99.55	19.68	45.10	54.77	53.35	99.56	76.45
MLS [26]	51.60	62.29	56.94	99.55	19.64	45.10	54.76	53.34	99.56	76.45
DICE [59]	59.34	68.38	63.86	99.56	27.24	59.65	62.15	52.39	99.28	75.84

Table 15. Results from the OASIS-3 benchmark for the AUROC and FPR@95 metrics.

	Modality	cs-ID		near-OOD				far-OOD	
		Scanner	Avg	ATLAS	BraTS	CT	Avg	MSD-H	CHAOS
<b>AUROC↑</b>									
MDSEns [40]	100.00	100.00	100.00	98.47	99.98	99.94	99.46	100.00	100.00
ViM [70]	100.00	97.63	98.82	98.19	97.01	100.00	98.40	100.00	100.00
Residual [70]	100.00	93.94	96.97	95.38	94.72	100.00	96.70	100.00	100.00
MDS [40]	100.00	92.62	96.31	94.65	93.80	100.00	96.15	100.00	100.00
KNN [61]	100.00	97.56	98.78	96.25	96.71	100.00	97.66	100.00	100.00
SHE [76]	97.20	86.51	91.85	85.03	87.37	100.00	90.80	99.28	100.00
RMDS [52]	63.91	52.09	58.00	58.88	56.72	99.46	71.69	99.78	100.00
Relation [35]	31.28	59.68	45.48	67.20	53.23	78.16	66.20	86.55	99.26
fDBD [44]	47.96	69.27	58.62	74.38	64.59	86.96	75.31	91.02	94.84
SCALE [71]	99.96	69.11	84.53	63.25	89.70	100.00	84.32	96.46	100.00
ReAct [60]	31.99	57.49	44.74	54.15	67.86	88.69	70.23	64.61	90.45
ASH [15]	92.53	48.88	70.71	57.64	75.81	96.12	76.52	86.82	96.13
RankFeat [58]	81.54	61.03	71.29	60.10	66.14	97.72	74.65	93.98	100.00
OpenMax [8]	37.81	49.56	43.69	58.97	54.48	44.35	52.60	68.56	72.38
ODIN [42]	55.01	52.00	53.51	34.86	51.09	92.63	59.53	42.76	74.49
GEN [46]	19.36	54.54	36.95	63.28	49.29	47.94	53.50	77.18	79.71
MSP [23]	19.36	54.54	36.95	63.28	49.29	47.94	53.50	77.18	79.71
Dropout [17]	19.69	54.52	37.10	62.32	49.31	48.02	53.22	74.70	79.56
TempScale [19]	19.36	54.54	36.95	63.28	49.29	47.94	53.50	77.18	79.71
NNGuide [49]	24.16	45.36	34.76	48.43	56.79	65.63	56.95	57.32	95.43
KLM [24]	61.10	47.92	54.51	54.38	46.71	32.38	44.49	64.89	63.08
EBO [45]	19.80	47.92	33.86	55.77	51.37	41.02	49.39	63.70	75.60
MLS [26]	19.80	48.07	33.94	56.01	51.34	41.05	49.47	63.92	75.54
DICE [59]	32.67	36.66	34.66	18.32	27.82	32.27	26.14	20.88	26.52
<b>FPR@95↓</b>									
MDSEns [40]	0.00	0.00	0.00	0.00	0.00	0.00	0.00	0.00	0.00
ViM [70]	0.00	11.05	5.52	8.29	13.81	0.00	7.37	0.00	0.00
Residual [70]	0.00	19.34	9.67	12.15	20.44	0.00	10.87	0.00	0.00
MDS [40]	0.00	22.10	11.05	15.47	22.10	0.00	12.52	0.00	0.00
KNN [61]	0.00	13.81	6.91	14.92	17.68	0.00	10.87	0.00	0.00
SHE [76]	4.97	35.91	20.44	32.60	30.94	0.00	21.18	2.21	0.00
RMDS [52]	95.58	98.90	97.24	89.50	91.71	0.00	60.41	2.21	0.00
Relation [35]	82.32	82.32	82.32	91.16	50.28	74.59	42.54	11.60	27.07
fDBD [44]	67.40	75.69	71.55	75.69	75.69	21.55	57.64	21.55	11.05
SCALE [71]	0.00	83.98	41.99	82.87	57.46	0.00	46.78	13.26	0.00
ReAct [60]	86.74	83.98	85.36	75.69	81.22	37.02	64.64	55.80	37.57
ASH [15]	18.78	86.19	52.49	91.71	71.82	3.87	55.80	23.76	3.87
RankFeat [58]	50.83	74.59	62.71	65.75	81.22	13.81	53.59	18.23	0.00
OpenMax [8]	86.19	87.29	86.74	87.29	81.77	86.19	85.08	71.82	59.67
ODIN [42]	64.09	83.43	73.76	86.74	76.80	47.51	70.35	79.56	65.19
GEN [46]	91.16	86.74	88.95	85.64	89.50	85.64	86.92	63.54	43.65
MSP [23]	91.16	86.74	88.95	85.64	89.50	85.64	86.92	63.54	43.65
Dropout [17]	90.06	87.29	88.67	85.64	90.06	85.64	87.11	69.06	41.44
TempScale [19]	91.16	86.74	88.95	85.64	89.50	85.64	86.92	63.54	43.65
NNGuide [49]	87.85	87.85	87.85	88.40	87.85	79.56	85.27	70.72	27.62
KLM [24]	82.87	97.24	90.06	93.37	96.13	97.24	95.58	74.59	79.01
EBO [45]	88.40	87.85	88.12	88.40	87.85	87.85	88.03	75.69	47.51
MLS [26]	88.40	87.85	88.12	88.40	87.85	87.85	88.03	75.69	47.51
DICE [59]	77.35	91.71	84.53	92.27	85.64	83.43	87.11	85.64	80.11

Table 16. Results from the OASIS-3 benchmark for the AUPR<sub>IN</sub> and AUPR<sub>OUT</sub> metrics.

	Modality	cs-ID		near-OOD				far-OOD	
		Scanner	Avg	ATLAS	BraTS	CT	Avg	MSD-H	CHAOS
<b>AUPR<sub>IN</sub>↑</b>									
MDSEns [40]	100.00	100.00	100.00	85.77	99.89	99.22	94.96	100.00	100.00
ViM [70]	100.00	98.95	99.47	95.50	89.45	100.00	94.99	100.00	100.00
Residual [70]	100.00	97.54	98.77	93.47	87.17	100.00	93.55	100.00	100.00
MDS [40]	99.99	96.98	98.49	92.51	85.57	100.00	92.69	100.00	100.00
KNN [61]	100.00	98.93	99.46	92.93	88.62	100.00	93.85	100.00	100.00
SHE [76]	96.87	94.27	95.57	79.70	73.60	100.00	84.43	99.92	100.00
RMDS [52]	29.10	66.63	47.86	30.23	15.79	93.64	46.55	99.98	100.00
Relation [35]	31.03	78.53	54.78	38.63	17.06	61.19	38.96	98.31	99.92
fDBD [44]	47.17	84.04	65.60	53.32	32.83	82.61	56.25	98.99	99.50
SCALE [71]	99.87	80.84	90.35	38.98	53.18	100.00	64.05	99.56	100.00
ReAct [60]	27.46	78.03	52.74	42.07	32.32	72.90	49.09	95.20	98.96
ASH [15]	89.95	71.72	80.84	31.09	37.84	96.53	55.15	98.49	99.64
RankFeat [58]	70.72	81.47	76.09	51.59	27.79	91.86	57.08	99.32	100.00
OpenMax [8]	30.53	72.16	51.35	36.66	27.72	23.74	29.37	95.14	96.69
ODIN [42]	52.11	74.82	63.47	28.22	25.26	68.08	40.52	90.52	96.72
GEN [46]	22.64	75.14	48.89	39.94	21.96	22.42	28.11	96.51	97.78
MSP [23]	22.64	75.14	48.89	39.94	21.96	22.42	28.11	96.51	97.78
Dropout [17]	22.98	74.85	48.92	39.64	22.01	22.36	28.00	95.96	97.73
TempScale [19]	22.64	75.14	48.89	39.94	21.96	22.42	28.11	96.51	97.78
NNGuide [49]	25.77	70.64	48.20	32.35	25.67	30.65	29.55	93.63	99.51
KLM [24]	37.68	67.45	52.56	28.05	13.92	8.57	16.85	93.85	95.10
EBO [45]	24.40	71.31	47.85	34.94	23.90	20.58	26.47	94.46	97.21
MLS [26]	24.40	71.34	47.87	35.00	23.89	20.58	26.49	94.49	97.20
DICE [59]	35.94	64.33	50.13	21.46	19.18	22.00	20.88	85.76	88.78
<b>AUPR<sub>OUT</sub>↑</b>									
MDSEns [40]	100.00	100.00	100.00	99.62	100.00	99.99	99.87	100.00	100.00
ViM [70]	100.00	95.15	97.57	99.38	99.47	100.00	99.62	100.00	100.00
Residual [70]	100.00	84.90	92.45	97.84	98.98	100.00	98.94	100.00	100.00
MDS [40]	100.00	81.85	90.92	97.29	98.80	100.00	98.70	100.00	100.00
KNN [61]	100.00	95.02	97.51	98.49	99.42	100.00	99.30	100.00	100.00
SHE [76]	98.02	64.90	81.46	91.83	96.74	100.00	96.19	93.65	100.00
RMDS [52]	86.94	38.65	62.80	82.12	89.86	99.93	90.64	98.26	100.00
Relation [35]	63.39	39.49	51.44	85.29	87.29	94.44	89.01	51.59	96.11
fDBD [44]	69.37	46.84	58.11	88.23	90.16	95.26	91.22	37.96	46.06
SCALE [71]	99.99	57.82	78.90	83.51	98.29	100.00	93.94	87.52	100.00
ReAct [60]	64.56	33.10	48.83	72.11	92.78	98.00	87.63	12.48	62.71
ASH [15]	93.33	29.72	61.52	79.04	92.54	97.22	89.60	28.04	50.43
RankFeat [58]	92.48	33.99	63.24	75.50	92.52	99.65	89.22	65.40	100.00
OpenMax [8]	71.23	31.98	51.60	80.94	87.99	83.90	84.28	15.20	25.35
ODIN [42]	73.04	38.14	55.59	63.73	84.36	98.93	82.34	8.04	30.43
GEN [46]	59.71	35.28	47.50	82.87	85.71	84.52	84.37	22.30	19.47
MSP [23]	59.71	35.28	47.50	82.88	85.72	84.52	84.38	22.30	19.47
Dropout [17]	59.83	34.32	47.07	81.86	85.23	84.50	83.86	21.52	21.96
TempScale [19]	59.71	35.28	47.50	82.88	85.72	84.52	84.38	22.30	19.47
NNGuide [49]	61.07	27.28	44.17	70.65	89.81	93.02	84.49	10.64	79.77
KLM [24]	76.10	29.95	53.03	76.91	83.39	80.44	80.25	13.72	11.59
EBO [45]	59.79	29.39	44.59	76.63	87.03	81.74	81.80	12.59	27.42
MLS [26]	59.79	29.82	44.80	77.23	86.94	81.74	81.97	12.68	24.82
DICE [59]	63.38	30.60	46.99	58.38	74.31	78.08	70.26	6.25	6.07

Table 17. Results from the ImageNet1k benchmark for the AUROC and FPR@95 metrics.

	cs-ID				near-OOD			far-OOD			
	IN-V2 [51]	IN-C [22]	IN-R [25]	Avg	SSB-hard [69]	NINCO [9]	Avg	iNaturalist [28]	Textures [13]	OpenImage-O [70]	Avg
<b>AUROC↑</b>											
MDSEns [40]	51.15	76.74	74.87	67.58	48.30	60.66	54.48	56.42	93.30	73.82	74.51
ViM [70]	57.34	83.77	87.95	76.35	65.53	78.63	72.08	89.56	97.97	90.50	92.68
Residual [70]	49.83	67.78	65.52	61.04	42.14	54.59	48.37	52.13	87.81	61.02	66.99
MDS [40]	51.72	70.80	69.78	64.10	48.50	62.38	55.44	63.67	89.80	69.27	74.25
KNN [61]	56.44	83.94	87.64	76.01	62.57	79.64	71.10	86.41	97.09	87.04	90.18
SHE [76]	57.60	83.65	86.18	75.81	68.73	82.79	75.76	95.40	97.16	91.57	94.71
RMDS [52]	58.70	79.70	81.73	73.38	71.77	82.22	76.99	87.24	86.08	85.84	86.38
Relation [35]	56.92	79.05	84.38	73.45	65.90	79.82	72.86	91.26	91.32	88.34	90.31
fDBD [44]	58.56	81.77	87.64	75.99	70.65	82.60	76.63	93.70	93.44	91.17	92.77
SCALE [71]	58.36	84.07	83.81	75.41	77.34	85.37	81.36	98.02	97.63	93.95	96.53
ReAct [60]	58.49	80.99	85.98	75.15	73.02	81.73	77.38	96.34	92.79	91.87	93.67
ASH [15]	58.07	83.85	84.15	75.36	74.71	84.54	79.63	97.72	97.87	93.82	96.47
RankFeat [58]	53.05	66.11	64.42	61.19	58.87	54.27	56.57	58.64	74.79	60.20	64.54
OpenMax [8]	58.07	80.10	85.69	74.62	71.37	78.17	74.77	92.05	88.10	87.62	89.26
ODIN [42]	57.60	76.19	85.47	73.09	71.74	77.77	74.75	91.17	89.00	88.23	89.47
GEN [46]	58.89	80.60	86.44	75.31	72.00	81.69	76.85	92.44	87.59	89.26	89.76
MSP [23]	58.54	77.06	80.51	72.04	72.09	79.95	76.02	88.41	82.43	84.86	85.23
Dropout [17]	58.51	76.97	80.41	71.96	71.99	79.81	75.90	88.21	82.26	84.64	85.04
TempScale [19]	58.89	78.78	83.16	73.61	72.87	81.41	77.14	90.50	84.95	87.22	87.56
NNGuide [49]	58.63	82.90	87.57	76.37	73.42	81.97	77.69	95.44	95.16	92.39	94.33
KLM [24]	57.57	76.77	81.64	71.99	71.40	81.91	76.65	90.79	84.71	87.30	87.60
EBO [45]	58.75	80.99	86.82	75.52	72.42	80.29	76.35	91.14	88.50	89.19	89.61
MLS [26]	58.77	80.93	86.70	75.46	72.51	80.41	76.46	91.17	88.39	89.17	89.57
DICE [59]	57.01	80.19	80.38	72.53	72.91	77.56	75.23	94.56	92.28	88.61	91.81
<b>FPR@95↓</b>											
MDSEns [40]	93.49	78.06	67.45	79.67	93.47	84.65	89.06	81.54	34.07	71.69	62.43
ViM [70]	92.14	65.75	46.55	68.15	80.41	62.28	71.35	30.69	10.49	32.82	24.67
Residual [70]	94.34	82.00	77.94	84.76	96.93	89.96	93.45	89.61	53.62	86.53	76.59
MDS [40]	93.40	75.47	71.00	79.96	92.10	78.80	85.45	73.81	42.79	72.15	62.92
KNN [61]	92.81	68.14	53.23	71.39	83.36	58.39	70.87	40.80	17.31	44.27	34.13
SHE [76]	92.31	65.04	51.32	69.56	79.56	54.20	66.88	20.78	15.57	33.29	23.21
RMDS [52]	91.66	72.44	59.37	74.49	77.88	52.20	65.04	33.67	48.80	40.27	40.91
Relation [35]	92.22	75.78	62.74	76.91	86.50	59.92	73.21	32.94	33.61	41.66	36.07
fDBD [44]	92.03	69.80	50.46	70.76	77.28	52.08	64.68	22.02	27.71	29.93	26.55
SCALE [71]	91.24	67.63	62.02	73.63	67.72	51.86	59.79	9.52	11.91	28.13	16.52
ReAct [60]	91.92	74.40	53.71	73.34	77.55	55.88	66.72	16.70	29.65	32.57	26.31
ASH [15]	91.29	66.91	62.12	73.44	70.81	53.11	61.96	10.99	11.01	28.61	16.87
RankFeat [58]	93.18	83.82	80.79	85.93	87.41	88.28	87.85	81.56	69.95	81.77	77.76
OpenMax [8]	91.59	73.88	51.32	72.27	77.33	60.81	69.07	25.29	40.26	37.39	34.31
ODIN [42]	92.51	79.99	59.46	77.32	76.83	68.16	72.50	35.98	49.24	46.66	43.96
GEN [46]	91.95	74.35	54.37	73.56	75.72	54.89	65.31	26.09	46.26	34.53	35.63
MSP [23]	91.85	77.54	66.24	78.54	74.48	56.85	65.66	43.35	60.86	50.16	51.46
Dropout [17]	91.67	77.52	65.92	78.37	74.58	57.31	65.94	43.72	61.72	50.57	52.00
TempScale [19]	91.76	77.24	63.31	77.44	73.90	55.13	64.52	37.56	56.94	45.43	46.65
NNGuide [49]	91.61	72.16	53.18	72.32	74.70	56.85	65.77	20.36	26.02	31.98	26.12
KLM [24]	92.85	83.54	72.56	82.98	84.73	59.61	72.17	38.49	52.29	48.80	46.52
EBO [45]	91.93	74.88	53.46	73.42	76.27	59.83	68.05	30.49	46.27	37.79	38.19
MLS [26]	91.95	74.65	53.61	73.40	76.20	59.44	67.82	30.61	46.17	37.88	38.22
DICE [59]	91.79	75.54	62.68	76.67	75.86	66.26	71.06	25.83	42.80	48.50	39.04

Table 18. Results from the ImageNet1k benchmark for the  $AUPR_{IN}$  and  $AUPR_{OUT}$  metrics.

	cs-ID				near-OOD			far-OOD			
	IN-V2 [51]	IN-C [22]	IN-R [25]	Avg	SSB-hard [69]	NINCO [9]	Avg	iNaturalist [28]	Textures [13]	OpenImage-O [70]	Avg
<b>AUPR<sub>IN</sub>↑</b>											
MDSEns [40]	82.96	91.56	82.45	85.66	48.23	92.32	70.28	87.13	98.47	88.79	91.46
ViM [70]	85.14	95.03	91.50	90.56	65.67	96.49	81.08	97.59	99.74	96.58	97.97
Residual [70]	82.20	90.00	75.91	82.70	42.63	90.66	66.65	84.35	98.17	81.52	88.01
MDS [40]	83.11	91.37	79.81	84.76	49.37	93.24	71.30	89.91	98.60	87.35	91.95
KNN [61]	84.66	95.01	90.80	90.16	62.33	96.74	79.53	96.66	99.61	95.04	97.10
SHE [76]	85.13	95.15	90.40	90.23	67.41	97.28	82.35	98.80	99.64	96.82	98.42
RMDS [52]	85.56	93.71	87.13	88.80	69.90	97.24	83.57	97.02	97.98	94.82	96.61
Relation [35]	84.78	93.24	87.87	88.63	62.79	96.69	79.74	97.85	98.85	95.55	97.42
fDBD [44]	85.44	94.32	91.02	90.26	69.62	97.31	83.46	98.56	99.14	96.90	98.20
SCALE [71]	85.61	94.98	87.51	89.36	76.95	97.64	87.29	99.54	99.69	97.67	98.97
ReAct [60]	85.46	93.74	89.58	89.59	70.70	97.06	83.88	99.14	99.03	96.96	98.37
ASH [15]	85.50	94.94	87.63	89.36	74.47	97.48	85.98	99.47	99.73	97.61	98.94
RankFeat [58]	83.55	89.31	74.24	82.37	57.98	90.77	74.38	87.67	96.08	82.64	88.79
OpenMax [8]	85.31	93.75	89.93	89.66	70.13	96.42	83.28	98.19	98.40	95.57	97.39
ODIN [42]	85.11	92.17	88.58	88.62	70.52	96.13	83.33	97.72	98.21	95.23	97.05
GEN [46]	85.61	93.73	89.71	89.68	71.25	97.11	84.18	98.23	98.13	96.11	97.49
MSP [23]	85.54	92.60	85.22	87.78	71.50	96.76	84.13	97.09	97.18	94.11	96.13
Dropout [17]	85.55	92.57	85.15	87.76	71.40	96.74	84.07	97.04	97.15	94.01	96.07
TempScale [19]	85.62	93.08	86.96	88.55	72.15	97.02	84.59	97.67	97.58	95.09	96.78
NNGuide [49]	85.60	94.39	90.37	90.12	72.37	97.06	84.72	98.89	99.28	97.09	98.42
KLM [24]	84.74	91.99	84.76	87.17	66.68	97.00	81.84	97.41	97.63	94.63	96.55
EBO [45]	85.56	93.77	89.92	89.75	71.27	96.79	84.03	97.87	98.25	95.97	97.36
MLS [26]	85.56	93.75	89.86	89.73	71.34	96.81	84.07	97.88	98.24	95.96	97.36
DICE [59]	85.14	93.57	85.75	88.15	71.56	96.15	83.85	98.61	98.74	95.26	97.54
<b>AUPR<sub>OUT</sub>↑</b>											
MDSEns [40]	18.13	51.08	61.55	43.59	49.72	14.67	32.19	19.39	74.53	47.45	47.12
ViM [70]	21.97	60.77	79.98	54.24	63.24	29.11	46.18	59.24	88.60	74.43	74.09
Residual [70]	17.71	30.25	49.77	32.57	45.90	12.15	29.02	18.30	56.39	34.43	36.37
MDS [40]	18.37	32.54	53.23	34.71	49.36	14.55	31.96	23.28	57.96	40.03	40.42
KNN [61]	21.68	66.29	82.29	56.75	61.97	32.07	47.02	56.41	87.84	70.98	71.74
SHE [76]	22.45	61.99	78.42	54.28	68.82	38.62	53.72	84.83	85.49	79.59	83.31
RMDS [52]	22.92	47.28	70.59	46.93	70.70	31.93	51.31	50.31	45.81	61.60	52.58
Relation [35]	22.87	56.09	78.43	52.46	66.04	31.31	48.68	69.45	57.85	70.18	65.83
fDBD [44]	23.64	59.90	81.67	55.07	69.13	34.62	51.87	75.23	68.31	75.48	73.01
SCALE [71]	23.11	65.10	77.30	55.17	76.51	46.66	61.59	92.35	87.69	86.05	88.70
ReAct [60]	23.54	60.14	78.41	54.03	73.13	38.68	55.91	86.41	66.02	80.52	77.65
ASH [15]	22.88	64.69	78.18	55.25	73.88	44.73	59.31	91.31	88.56	85.68	88.52
RankFeat [58]	19.29	28.12	50.22	32.54	58.81	12.49	35.65	21.76	27.58	31.98	27.11
OpenMax [8]	22.68	45.87	73.70	47.42	69.52	26.64	48.08	63.57	37.49	61.82	54.29
ODIN [42]	22.90	51.31	81.18	51.80	71.05	32.73	51.89	72.11	61.00	73.72	68.95
GEN [46]	23.99	55.83	79.52	53.11	69.90	31.74	50.82	71.07	45.50	69.78	62.12
MSP [23]	23.61	51.40	73.00	49.34	70.34	31.17	50.76	63.88	40.27	64.60	56.25
Dropout [17]	23.49	51.04	72.81	49.12	70.22	31.04	50.63	63.51	39.75	64.18	55.81
TempScale [19]	23.95	54.76	76.33	51.68	70.96	32.42	51.69	67.17	44.86	68.06	60.03
NNGuide [49]	23.60	64.80	82.37	56.93	72.98	39.73	56.36	84.55	81.21	82.23	82.66
KLM [24]	23.15	46.91	73.33	47.80	72.54	35.77	54.16	70.16	36.45	68.81	58.47
EBO [45]	23.91	59.66	80.68	54.75	71.03	31.39	51.21	66.31	53.59	71.63	63.84
MLS [26]	23.94	59.20	80.41	54.52	71.10	31.60	51.35	66.61	52.74	71.46	63.60
DICE [59]	21.88	57.70	71.42	50.34	72.91	34.49	53.70	82.84	73.85	77.05	77.92

Table 19. Overview of the hyperparameter ranges for each OOD detection method with tunable hyperparameters employed in this work.

Method	Parameter 1	Parameter Range	Parameter 2	Parameter Range
MDSEns	noise	[0, 0.0025, 0.0014, 0.005, 0.01, 0.02, 0.04, 0.08]	–	–
ViM	dim	[1, 16, 32, 64, 128, 256]	–	–
Residual	dim	[32, 64, 128, 256, 512, 1024]	–	–
KNN	k	[1, 2, 5, 10, 25, 50, 100, 200, 500, 750, 1000]	–	–
SHE	metric	[inner product, euclidean, cosine]	–	–
Relation	pow	[1, 2, 4, 6, 8]	–	–
fDBD	normalized	[False, True]	–	–
SCALE	percentile	[65, 70, 75, 80, 85, 90, 95]	–	–
ReAct	percentile	[85, 90, 95, 99]	–	–
ASH	percentile	[65, 70, 75, 80, 85, 90, 95]	–	–
RankFeat	acc	[False, True]	temp	[0.1, 1, 10, 100, 1000]
OpenMax	sampling ratio	[0.01]	neighbors	[9]
ODIN	temperature	[1, 10, 100, 1000]	noise	[0.0014, 0.0028]
GEN	gamma	[0.01, 0.1, 0.5, 1, 2, 5, 10]	M	[1, 2, 3, 4, 5, 6, 7, 50, 100, 200]
Dropout	p	[0.5]	times	[15]
NNGuide	k	[1, 2, 5, 10, 50, 100, 200, 500, 750]	alpha	[0.01, 0.1, 0.25, 0.5, 0.75, 1.0]
EBO	temperature	[0.1, 0.5, 1, 1.5, 2.0]	–	–
DICE	percentile	[60, 65, 70, 75, 80, 85, 90, 95]	–	–

Table 20. Overview of the automatically selected hyperparameters for the three MIBs and ImageNet1k.

Method	MIDOG		PhaKIR		OASIS-3		ImageNet1k	
	Parameter 1	Parameter 2						
MDSEns	0.0	–	0.0014	–	0.0	–	0.0	–
ViM	256	–	256	–	256	–	256	–
Residual	128	–	128	–	64	–	1024	–
KNN	5	–	50	–	5	–	200	–
SHE	cosine	–	cosine	–	cosine	–	cosine	–
Relation	8	–	8	–	8	–	1	–
fDBD	False	–	False	–	True	–	True	–
SCALE	65	–	65	–	95	–	85	–
ReAct	95	–	90	–	85	–	95	–
ASH	65	–	65	–	95	–	85	–
RankFeat	False	0.1	True	10	False	1	True	0.1
OpenMax	0.01	9	0.01	9	0.01	9	0.01	9
ODIN	1	0.0014	1	0.0014	10	0.0028	10	0.0014
GEN	0.01	2	0.01	2	0.01	1	0.01	100
Dropout	0.5	15	0.5	15	0.5	15	0.5	15
NNGuide	1	0.1	5	0.01	5	0.01	500	0.01
EBO	2.0	–	0.1	–	0.1	–	0.5	–
DICE	85	–	95	–	80	–	65	–